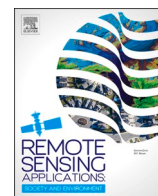


Contents lists available at [ScienceDirect](https://www.sciencedirect.com)

Remote Sensing Applications: Society and Environment

journal homepage: www.elsevier.com/locate/rsase

Impact assessment of humanitarian demining using object-based peri-urban land cover classification and morphological building detection from VHR Worldview imagery

Jennifer Killeen^{a,1}, Luan Jaupi^b, Brian Barrett^{a,*}^a School of Geographical & Earth Sciences, University of Glasgow, Glasgow, G128QQ, Scotland, UK^b The HALO Trust, Carronfoot, Thornhill, Dumfries, DG3 5BF, Scotland, UK

ARTICLE INFO

Keywords:

Building detection
Morphological building index
Landmine clearance
Afghanistan
Object-Based Image Analysis

ABSTRACT

This study utilised very high-resolution (VHR) imagery to monitor and evaluate the impact of humanitarian demining activities in a peri-urban environment in Afghanistan. Identifying buildings and mapping the spatial distribution of different types of land cover is of great practical significance for demining organisations, such as the HALO Trust, to assess the impact of their mine-clearance activities, by quantifying change and the growth of a population in a specific area over time. This study had two main objectives: (i) to map the post-clearance land cover, and (ii) to detect and quantify the change in the number and area of buildings. Two independent workflows were implemented and evaluated. To map land cover, this study investigated the implementation of various machine learning algorithms in object-based image classification (OBIA) of VHR satellite imagery (Worldview-1,2,3). Image segmentation was carried out using the Large-Scale Mean-Shift (LSMS) algorithm, before classification was performed based on a machine learning Random Forests (RF) approach. Different parameters and spatial distribution of training samples were tested to analyse the model's performance. Further analysis determined that by using only the segments' mean value per spectral band (Red, Green, Blue), data redundancy in the training stage was eliminated. The final classified map had an overall accuracy of 90.67% and a total built-area of 643,660.28 m² was detected in the 4.11 km² study area. To detect and quantify buildings present in the study area, an alternative, automatic, unsupervised approach based on the morphological building index (MBI) was implemented using MATLAB. Two VHR (0.5 m) panchromatic images acquired by WorldView-1 in 2008 and 2018 were processed using a series of multi-scale and multi-directional morphological operators, before a series of post-processing thresholds were applied to refine the output. Parameters were systematically optimised for the datasets and their sensitivity analysed. By comparing the output to manually labelled reference maps, producer's and user's accuracy of 78.63/81.70% and 75.30/77.91% were attained for 2008 and 2018 imagery respectively. The built-area was found to increase from 58,705 to 611,920 m² over the ten-year period, indicating a significant increase in the number of people resident in the area. Whilst OBIA was found to be more accurate than MBI for the 2018 pansharpened imagery, with producer's and user's accuracy of 91.00/90.60% versus 84.65/79.44% respectively, it must be considered that the MBI, an unsupervised method requiring no training, offers a fast solution if the sole objective is building detection.

* Corresponding author.

E-mail address: brian.barrett@glasgow.ac.uk (B. Barrett).¹ Present address: 2Excel geo, The Tiger House, Sywell Aerodrome, Sywell, Northampton, NN6 0BN, UK.<https://doi.org/10.1016/j.rsase.2022.100766>

Received 11 November 2021; Received in revised form 6 April 2022; Accepted 25 April 2022

Available online 6 May 2022

2352-9385/© 2022 The Authors. Published by Elsevier B.V. This is an open access article under the CC BY license (<http://creativecommons.org/licenses/by/4.0/>).

1. Introduction

Landmines maintain their potency to maim or kill long after they have been laid and until the mine is either neutralised or detonated. They can be found on roads, paths, farmer's fields, forests and near surrounding dwellings and other places where people are carrying out their daily activities. Landmines and other explosive remnants of war (ERW) such as unexploded ordnance (UXO) have a negative effect on physical security and health, economic productivity, and food security (Frost et al., 2017). Cultivable land is abandoned to avoid mine related death or injury and livestock are often lamed or killed, significantly impacting upon livelihoods. The wider long-term effects of landmines are a social and economic burden to victims, their families and the wider communities. Internally displaced populations (IDPs) and returning refugees to areas of ongoing or recent conflict are often those that are most at risk.

From 1979 to 2001, during the Soviet occupation and the civil war, Afghanistan was heavily mined by Soviet forces, the Afghan government pro-communist forces, insurgent resistance groups known collectively as the Mujahideen, the Taliban and the Northern Alliance. Many areas were mined by different groups at different times, leading to dense and complex ERW contamination. Millions of Afghans fled the country during this time, however many have since returned. Since 2001, ongoing conflict between government forces and armed opposition groups using victim-operated improvised explosive devices (IEDs), continued to contaminate Afghanistan and significantly impact civilian life. Consequently, Afghanistan became one of the most mined countries in the world, with estimates of up to 640,000 landmines laid since 1979, including huge amounts of UXO; more than 31,000 reported casualties were recorded between 1979 and 2018, although the actual total is certainly higher (The HALO Trust, 2020).

After clearance of landmines and other hazardous debris of war such as unexploded ordnance (UXO), there is a need to quantify the scale at which the cleared land is used and for what purposes. For monitoring and evaluation purposes humanitarian demining agencies such as The HALO Trust are interested not only in the number of people using the land after clearance, but also for what use and whether this land use changes over time. One of the most effective and safest ways to do this is to use satellite imagery (before and after clearance) to demonstrate the impact of the clearance work. Various remote sensing approaches have been explored for detecting landmine contaminated areas, including multispectral (e.g. Maathuis, 2003), hyperspectral (e.g. Makki et al., 2017), thermal (e.g. Kaya and Leloglu, 2017), Synthetic Aperture Radar (SAR) (e.g. Fernández et al., 2018) and in the assessment of these areas post-clearance (e.g. Cruz et al., 2018; Ibrahim et al., 2021). For automated and accurate building detection in landmine cleared areas, commercial, multispectral, VHR (less than 1 m spatial resolution) satellite imagery can hold great potential. The increased spatial resolution causes a higher intra-class and lower inter-class spectral variance, as real-world objects are represented by many pixels with different spectral reflectance; thus, the spectral separability of similar classes is reduced (Weng et al., 2018). Furthermore, due to the complexity and diversity of building structures, extraction of buildings from VHR imagery still faces challenges in terms of accuracy and efficiency, and remains a hot research topic in the fields of photogrammetry, RS and computer vision (Weng et al., 2018).

The advantages of different methods of building detection, such as visual interpretation, pixel-based classification, OBIA, and mathematical morphology are summarised in Table 1a. OBIA is a key field of research for building extraction from VHR imagery. However, many challenges remain such as determining the optimum segmentation algorithm and associated parameters, the inaccurate spatial relationship between real-world objects and segments (Lhomme et al., 2009; Ma et al., 2017a,b), and over-/under-segmentation. Furthermore, OBIA relies on a supervised classification which requires many training samples. Due to higher intra-class and lower inter-class variance of features in VHR imagery, the potential accuracy of pixel-based classification is decreased due to the 'salt and pepper effect' (Blaschke et al., 2000). One of the key advantages of classifying segments rather than pixels, is to overcome this effect (Blaschke, 2010). Many studies have compared pixel- and object-based classifications of high-resolution imagery for land cover mapping applications and have shown that object-based approaches provide higher accuracy (Cleve et al., 2008; Bhaskaran et al., 2010; Galletti and Myint, 2014). Conversely, building indices provide an alternative unsupervised approach to building detection, by exploiting the low spectral variation within the building structure and high spectral variation corresponding to the building periphery. The MBI is a feature index, based on mathematical morphology, that aims to automatically and accurately detect buildings in VHR imagery, without any training or segmentation process (Huang and Zhang, 2011).

Various extensions to the original MBI were developed aiming to reduce commission and omission errors from dark and heterogeneous roofs, roads, and bare soil (Huang and Zhang, 2012). Shadows extracted from the complimentary morphological shadow

Table 1a
Summary of building detection methods, amended after Wang et al. (2016).

Method	Advantages	Disadvantages
Visual interpretation	<ul style="list-style-type: none"> Possible to accurately count objects Can produce reference maps when survey data is not available 	<ul style="list-style-type: none"> Time-consuming Labour intensive
Pixel-based classification	<ul style="list-style-type: none"> Relatively simple to implement Most software (open-source/commercial) provides this functionality 	<ul style="list-style-type: none"> Requires prior-knowledge of study area Sensitive to training data (supervised classification only)
OBIA	<ul style="list-style-type: none"> Processing performed on segments rather than pixels. Segments can be attributed with more than spectral information (e.g. spatial, textural, etc.) 	<ul style="list-style-type: none"> Requires prior-knowledge of study area Requires sufficient quantity and quality of training data
Mathematical morphology	<ul style="list-style-type: none"> Requires less prior-knowledge than pixel-based classification or OBIA Fast processing 	<ul style="list-style-type: none"> Not able to detect objects without clearly defined shape or sufficient spectral contrast to surroundings

index (MSI) were used as a spatial constraint for building candidates, whilst a geometric index was defined to better discriminate between roads and buildings. Experiments performed on Ikonos/WorldView-2 imagery (1/2 m spatial resolution) showed the new method achieved high accuracy (OA: 91.1%) for discrimination between buildings and background features and improved upon the original MBI (OA: 87.5%). The applicability of the method was later extended from urban areas to large, complex, VHR scenes in suburban, rural, mountainous and agricultural environments, through a systematic post-processing framework (Huang et al., 2017). The original MBI and its extensions have been shown to be fast, unsupervised methods for building detection, without the requirement of training samples. The method is fast and relatively simple to implement for large, complex scenes in VHR satellite imagery. It has been implemented across different applications, including building extraction (Zhang et al., 2016; Jiménez et al., 2017; Li et al., 2017; Xiangguo and Jixian, 2017; Ding et al., 2018; You et al., 2018; Ma et al., 2019; Bi et al., 2019), change detection (Tang et al., 2013; Huang et al., 2014), and urban planning (Wang et al., 2016) and been shown to produce more accurate results than previous building indices, such as the texture-derived built-up presence index (PanTex) (Pesaresi et al., 2008).

The aims of this research were i) to assess the impact of humanitarian demining by the HALO Trust in peri-urban areas in Afghanistan between 2008 and 2018 for monitoring and evaluation (M&E) purposes, by investigating how much of the land is being used after clearance and for what purposes, and ii) to develop a set of semi-automatic workflows to directly quantify several useful indicators from very high-resolution (VHR) satellite imagery, such as land cover (LC) and the number and area of buildings. The approaches are based on object-based image analysis (OBIA), including segmentation and supervised machine-learning (ML) classification, and morphological image analysis (MIA).

2. Methods

2.1. Study area

Jebrail ($34^{\circ} 22' 47''$ N $62^{\circ} 8' 12''$ E) is a suburb located a couple of kilometres north-west of the city of Herat in the Injil District in Herat Province in Afghanistan (Fig. 1a). The city lies on the ancient trade and communication routes of the Middle East, Central and Southern Asia, known as the Silk Roads. Today, Herat is a regional hub in western Afghanistan and is still strategically important for trade, with roads leading to Iran, Turkmenistan and other parts of Afghanistan. Since 2008, Jebrail has been fast-growing with hundreds of plots of lands being distributed or sold to people from various ethnic groups for housing. The environment is classed as peri-urban, as it sits in the transition area between rural areas and the outer limits of the urban centre of Herat. Jebrail has many hotels, stores, internet cafes, restaurants, mosques, bookshops, butchers, pharmacies, petrol stations, hospitals, nightclubs, electronics and mobile repair shops, libraries, etc. (Fig. 1b). There is a large customs parking lot, with many parked trucks, heavy goods vehicles



Fig. 1a. Location of the minefields cleared by the HALO Trust in Jebrail, to the north-west of the city of Herat in Afghanistan.

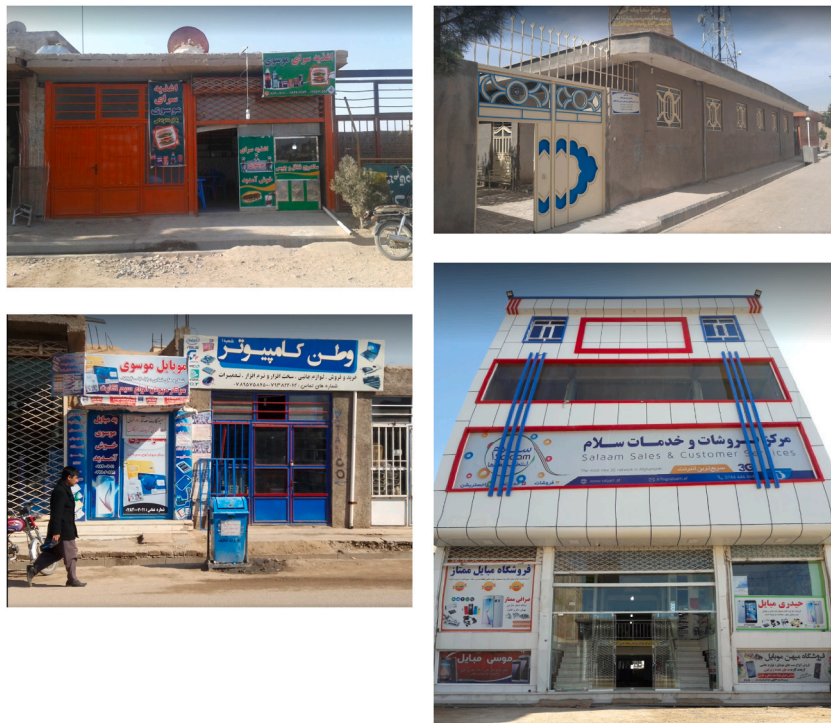


Fig. 1b. Stores and residences in Jebrail. This imagery gives context to the number of floors in buildings, the type and appearance of building materials and characteristics of the ground areas (i.e. bare soil and tarmac). Source: Google Maps.



Fig. 1c. Subset of 2017/2018/2019 pansharpened imagery, showing an area of approximately 0.025 km², to show different spatial resolutions, solar conditions and the impact of off-nadir angle on shadow geometry and off-nadir viewing of buildings. No image enhancement is applied. [Imagery source: U.S. Department of State © 2017, 2018, 2019, DigitalGlobe NextView License].

(HGVs) and containers, which serves Herat airport and the local Iranian border.

Since the first census in 1979, Afghanistan has not been able to carry out a population census, due to over three decades of war and conflict. Thus, the settled population of the country continues to be estimated based on the data obtained from the 2003–2005 Household Listing (HHL). The total population of Afghanistan in 2019 is estimated to be approximately 32.2 million (50.9% men, 49.1% women), with 71.4/23.9% living in rural/urban areas respectively, whilst the remaining 4.7% of the population is nomadic. The UN provides a slightly higher estimate of the 2019 population at 38.04 million (UN data, 2019). Herat is the third most populous city of Afghanistan, after Kabul and Kandahar. In 2019, 2,095,117 people were estimated to be settled in Herat Province, with 556,205 people in Herat City District and 271,717 in Injil District, where Jebrail is located. The population of the districts of Herat City and Injil are estimated to have increased during 2004–2019 due to returning refugees and IDPs.

Herat has pronounced ethnic segregation and Jebrail is now home to a minority population, predominantly Hazaras, of approximately 60,000 (United States Institute of Peace, 2015). The Hazaras are an ethnic minority group native to Hazārajāt, or Hazāristān, a mountainous region in central Afghanistan, who traditionally inhabited an old city quarter of Herat. Herat lies at 920 m elevation and

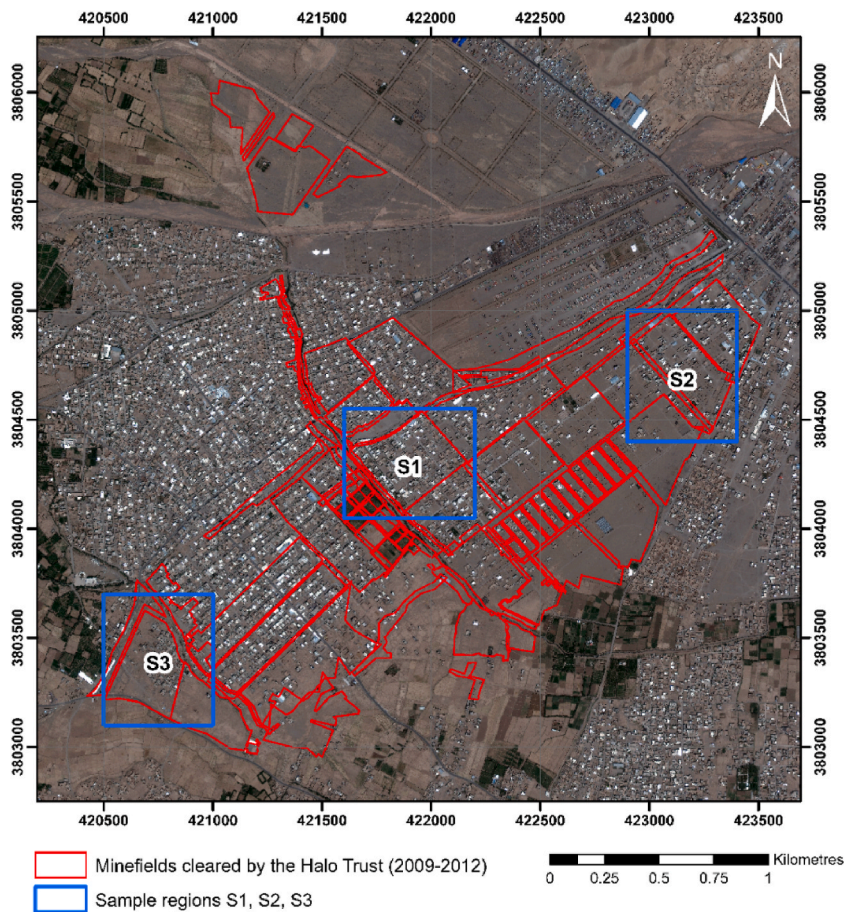


Fig. 1d. Pansharpened natural colour composite of Jebrail, Afghanistan, acquired by WorldView-3 on 17/07/2018. Red polygons indicate mine-clearance by the HALO Trust between 2009 and 2012 [Imagery source: U.S. Department of State © 2018 DigitalGlobe NextView License.]. (For interpretation of the references to colour in this figure legend, the reader is referred to the Web version of this article.)

has a cold, semi-arid climate. Temperatures lie within average lows/highs of $-2.9/9.1$ °C in January and $21.2/36.7$ °C in July, whilst precipitation is very low with an average of 0 mm falling between Jun–Sep, and 187.3 mm falling between Dec–Mar (NOAA, 2019). Please see Appendix A for information on mine clearance activities undertaken in Jebrail.

2.2. Datasets

This study used VHR imagery from DigitalGlobe’s (now part of Maxar Technologies) active series of WorldView-1/2/3 satellites. Sensor characteristics and imagery metadata are given in Table 2a & Table S1. Five cloud-free orthorectified images, including two panchromatic and three pansharpened images in GeoTIFF format, were downloaded from the DigitalGlobe G-EGD/EVWHS (Global-Enhanced GEOINT Delivery/EnhancedView Web-Hosting Services) portal by the HALO Trust.

A shapefile provided by the HALO Trust included 59 polygons, covering an area of 3,042,863 m², representing the areas in Jebrail that were cleared of mines between 2009 and 2012. The minefields were surveyed using a handheld GPS device (accuracy <10 m). Coordinates for landmarks were recorded and subsequently bearings and distances for the remaining extents of the minefield were measured using a compass with a laser-pointer. Differential GPS was too time-intensive, costly and dangerous to deploy in field. Due to the lower accuracy, the polygons overlap in some places, do not ‘fit’ together, and do not align with real-world features and boundaries in the georeferenced imagery. This was taken into account by using a 50 m buffer when LC metrics were derived from the analysis. No further detailed ground truth was available for the study, such as photographs or pre-existing thematic LC maps.

2.3. OBIA for land cover mapping

Orfeo ToolBox (OTB)(v6.6.1-Win64), an open-source library of tools for processing of RS imagery, developed by the French government space agency (Christophe and Inglada, 2009a, 2009b; Grizonnet et al., 2017; Cresson et al., 2018) was used in this study and implemented via MonteVerdi. Open-source GIS software, QGIS 3.6.2 ‘Noosa’ was used for geoprocessing and geovisualisation. Three pansharpened, natural colour composites were available for the OBIA stage of the project (Table 2a). The pansharpened images were acquired from 2017 to 2019 at the same time of year, within a six-week period in June/July, and at the same time of day (approx.

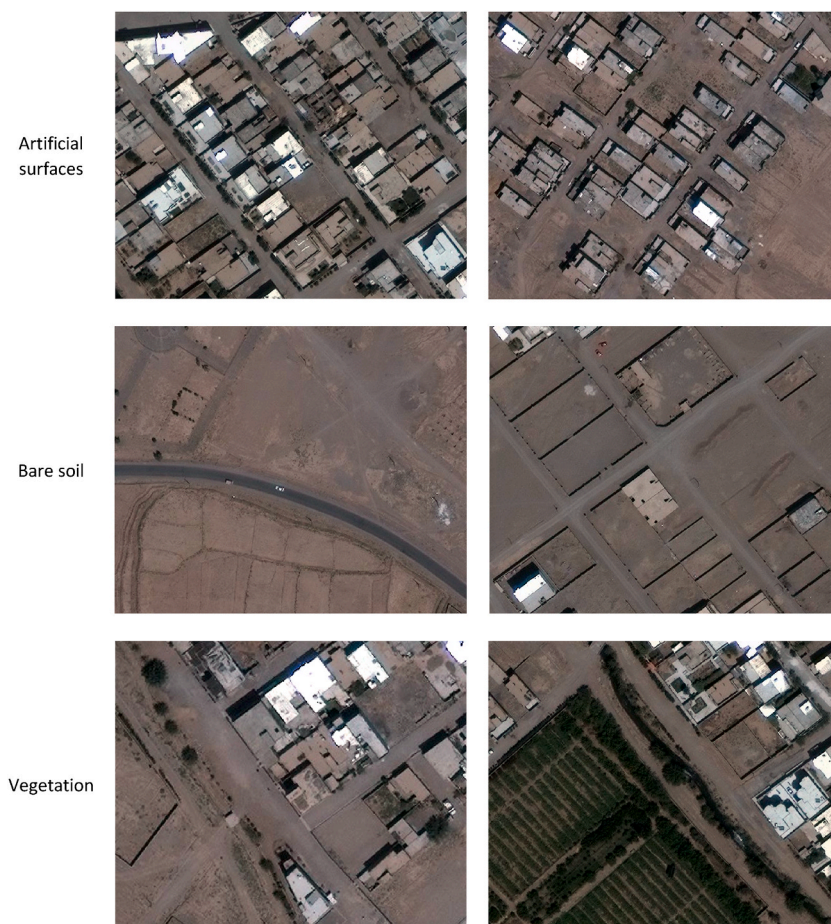


Fig. 1e. Examples of features labelled per the defined classification schema (artificial surfaces, bare soil, vegetation). Each image shows a mixture of features, since VHR imagery of urban areas tends to be complex. All the examples shown are taken from the 2018 pansharpened image, with 0.28 m spatial resolution. Specific examples for shadow areas are not shown, as they can be seen next to structures (e.g. buildings, fences, etc.) [Imagery source: U.S. Department of State © 2018 DigitalGlobe NextView License.].

11:30 a.m. local time (GMT+4:30)), enabling an annual comparison with respect to solar conditions (elevation and azimuth). The main difference between the images is the spatial resolution (0.46/0.28/0.30 m) and the off-nadir angle (28/22/15°). The imagery from 2018/2019 has a higher spatial resolution than 2017 (Fig. 1c) since they were acquired by WorldView-3 rather than WorldView-2. In practice, satellites do not collect imagery at nadir as they point at an angle to the observed area to increase the revisit times. A low off-nadir angle is desirable to minimise the building-lean effect (Fig. 1c). Since the clearance-activities finished in 2012, and after visual inspection there was not a significant change in LC between 2018 and 2019, the 2018 imagery was determined to be the optimum choice for analysis, based on having the highest spatial resolution and a low off-nadir angle.

2.3.1. Pre-processing

The OBIA workflow was implemented in four main steps: pre-processing, segmentation, classification and accuracy assessment. The orthorectified pansharpened true colour composites were provided with radiometric and atmospheric corrections applied. The imagery was subsequently reprojected to the local Cartesian CRS (EPSG: 32641) using cubic resampling, since this method is often used for continuous data such as satellite imagery. The pre-processed imagery was then clipped to the extent of the mine-clearance polygons, covering 12.25 km² (3.5 × 3.5 km) with a resampled GSD of 0.28 m. Three sample regions (S1, S2, S3) were extracted, each covering 0.3 km² (Fig. 1d). These sample regions were chosen as they encompassed a single mine-clearance polygon with different densities of new dwellings, as well as other LC classes of interest (i.e. vegetation). The sample regions were used for optimisation and evaluation of the segmentation step, and for collection of the samples for training/validation of the supervised classifiers, before the optimal workflow was implemented for the full scene.

2.3.2. Segmentation

A region-based segmentation algorithm, Large-Scale Mean-Shift (LSMS) (Michel et al., 2015) was implemented using OTB. Alternatives such as the standard mean-shift (MS) algorithm in OTB (Comaniciu and Meer, 2002) and the multi-resolution segmentation (MRS) in eCognition (Baatz and Schäpe, 2000) were also investigated. LSMS was selected over the original MS algorithm as tiling

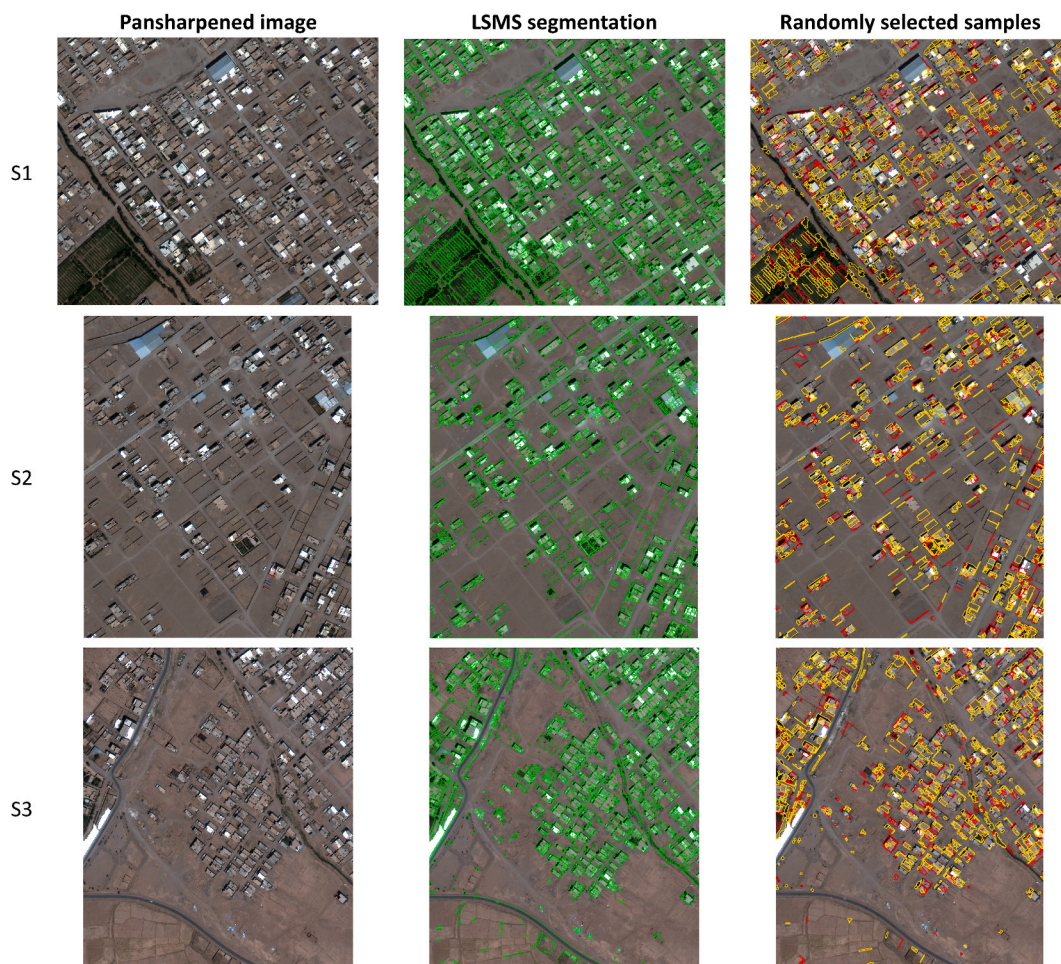


Fig. 1f. Three samples regions (S1/S2/S3) of the contrast enhanced 2018 pansharpened image. LSMS segmentation output is shown in the second column. The number of segments generated was dependent upon the scene's complexity (5388/2445/3043). Samples randomly selected for training (yellow) and validation (red) are shown in the third column. Each sample region represents an area of 0.3 km² [Imagery source: U.S. Department of State © 2018 DigitalGlobe NextView License.]. (For interpretation of the references to colour in this figure legend, the reader is referred to the Web version of this article.)

artefacts were removed and since it was specifically designed for processing large imagery. LSMS was selected over MRS, as it is an open-source and freely available.

The parameters for LSMS (5, 15, 100), were optimised through systematic trial-and-error. The 0.3 km² sample region S1 was represented by 5288 segments, whilst the full 12.25 km² scene was represented by 150,290 segments, taking a total of 3.5 h to process (on an Intel® Core™ i7-6500U CPU @ 2.50 GHz, 2601 MHz, 2 Cores, 4 Logical Processors; RAM 8 GB; System Type: x64-based PC). Even though each sample region covered the same area, the number of segments varied by almost 3000 in the case of S1 and S2, due to variable scene complexity (Fig. 1d). An advantage of using segments over pixels is that they have both additional spectral information (i.e. mean digital number (DN) value per band, variance, etc.) and spatial information (i.e. shape, size, texture, pattern, context, shadow, association, relative/absolute location, boundary conditions, topological relationships, etc.).

The LSMS algorithm computes two spectral attributes, the mean and the variance, by default. By using the segment's mean DN value, confusion in the classification stage is reduced, as the within-object variance is diminished. Further spectral statistics (mean, median, mode, minority, minimum, maximum, range, standard deviation, variance, variety) were computed for each segment based on the RGB spectral bands, with the aim of increasing the number of classification features available and potentially improving the classification accuracy. Geometric attributes, including area and perimeter, compactness and smoothness, were computed for each segment (Table 2b). Two shape index (SI) measures, compactness and smoothness, representing different ratios of the segment's area and perimeter, were computed. The height-to-width ratio (HWR) was computed from the orientated minimum bounding box for each segment.

2.3.3. Classification schema

Samples were selected for classification and accuracy assessment following a stratified random approach to ensure unbiased sample selection with a minimal number of samples per class of 380. Three LC classes were defined based on visual inspection of the imagery:

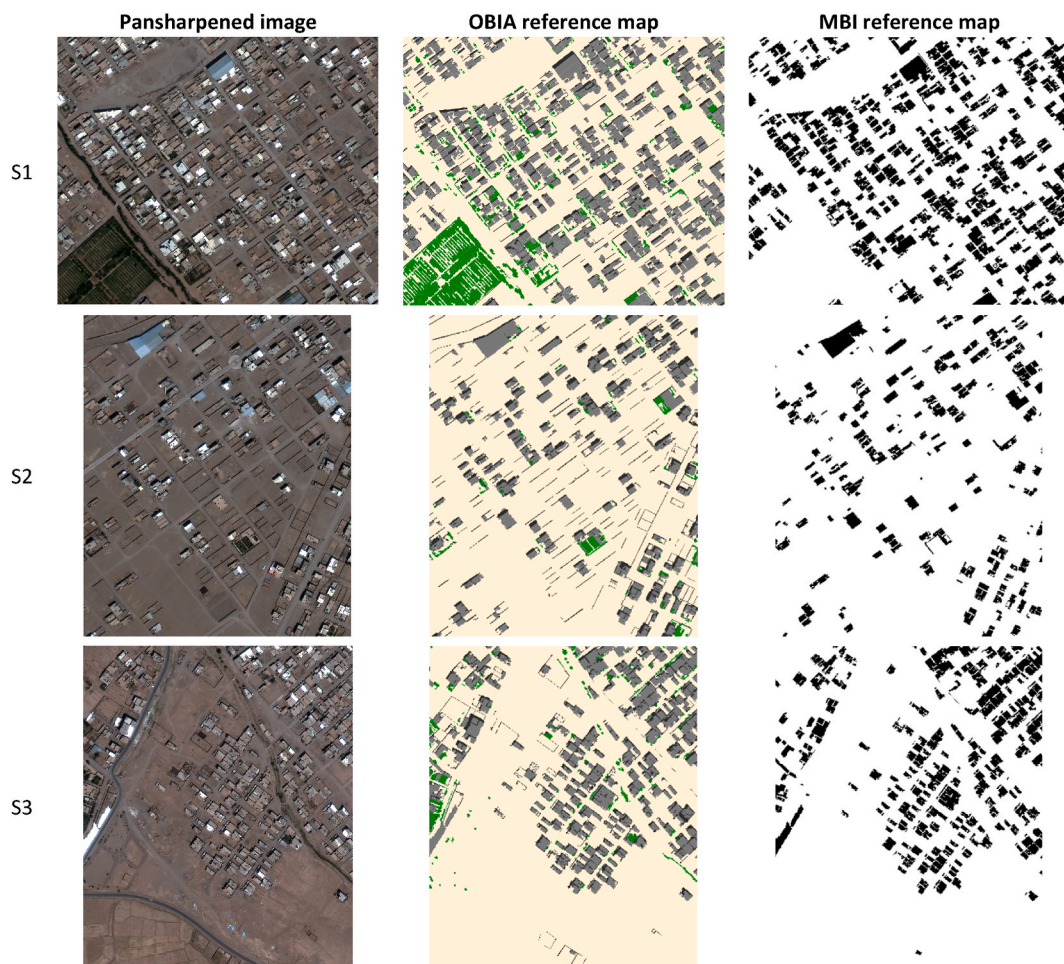


Fig. 1g. Reference maps for three samples regions (S1, S2, S3) of the 2018 pansharpended image, created for OBIA sampling scheme (second column) [Black = Shadow areas, Grey = Artificial surfaces, Beige = Bare soil, Green = Vegetation]. Reference maps were converted to binary building (black)/non-building (white) format (third column) for evaluation of the accuracy of MBI building map outputs. Each sample region represents an area of 0.3 km² [Imagery source: U.S. Department of State © 2018 DigitalGlobe NextView License.]. (For interpretation of the references to colour in this figure legend, the reader is referred to the Web version of this article.)

Table 2a

Imagery metadata. [*NIIRS, the *National Image Interpretability Rating Scale*, defines the quality of an image and its interpretability and is strongly linked to an image’s resolution (FAS, 2020)].

	Panchromatic		Pansharpended Natural Colour Composite		
Acquisition Date	08/10/2008	20/10/2018	10/06/2017	17/07/2018	08/06/2019
Local Time	09:24 p.m.	14:19 a.m.	11:28 a.m.	11:35 a.m.	11:28 a.m.
Source	WorldView-1	WorldView-1	WorldView-2	WorldView-3	WorldView-3
Source unit	Mosaic Product	Strip	Strip	Strip	Strip
GSD	50 cm	50 cm	50 cm	35 cm	33 cm
NIIRS*	–	4.80	4.80	5.50	5.60
Cloud Cover	0%	0%	0%	0%	0%
Cloudless geometry?	No	Yes	Yes	Yes	No
Off Nadir Angle	–	22.2608°	27.9660°	22.2560°	14.9296°
Sun Elevation	–	35.3216°	74.0729°	72.5351°	73.9819°
Sun Azimuth	–	221.4962°	130.9157°	135.3732°	131.4926°

i) Artificial surfaces (including tarmac, buildings, fences, etc.), ii) Bare soil (including natural material surfaces), iii) Vegetation (including trees, mixed soil/vegetation, etc.), along with a Shadow areas class. A water class was omitted, as there were no significant water bodies present in the imagery. Most roads were not tarmacked and were classed as bare soil, whilst tarmacked roads were classed as artificial surfaces, as well as all categories of building rooftops and structures. Examples of features per the classification schema are shown in Fig. 1e. Bare soil accounts for most of the ground area (≈80%), followed by artificial surfaces (≈10–14%),

Table 2b
Geometric features of image objects.

Feature	Description
Area	Area of segment, in m ² , calculated from the number of pixels multiplied by the square of the spatial resolution.
Perimeter	Perimeter of segment, in m.
Compactness (PP)	Compactness is given by a mathematical measure of the segment's shape, calculated via the Polsby-Popper Test for compactness (Polsby and Popper, 1991): $PP_i = \frac{4\pi \times Area_i}{Perimeter_i^2} \#1$ The perimeter of the segment is compared to the perimeter of a circle with the same area as the segment. PP can take a value within the interval [0, 1]. A score of 0 indicates a complete lack of compactness, whilst a score of 1 indicates maximal compactness, i.e. the segment is a perfect circle.
Smoothness (SI)	Smoothness of the segment's borders is given by the shape index (SI) which describes the similarity between the segment's borders and a perfect square. Fragmented objects will have a high SI. $SI_i = \frac{Perimeter_i \#2}{4\sqrt{Area_i}}$
Height/Width	The height/width ratio of the segment's orientated minimum bounding box is used to represent the length-width ratio of the segment. Isotropic segments will have a ratio close to 1, whilst anisotropic features that are long, narrow and elongated will have a high ratio. The QGIS tool <i>Orientated minimum bounding box</i> calculates the minimum area rotated rectangle that covers the segment.

Table 2c
Statistics for the training and validation samples per the pre-defined classes. *Due to a low proportion of vegetation in the peri-urban/suburban environment, a reduced number of samples was selected for this class.

Class	No. of segments			Total area, m ²	Mean segment area, m ²	Coverage, %
	Training	Validation	All			
Shadow areas	600	300	900	18,892.56	20.99	0.15
Artificial surfaces	600	300	900	26,116.67	29.02	0.21
Bare soil	600	300	900	29,501.21	32.78	0.24
Vegetation*	380	190	570	7209.84	12.65	0.06
Total	2180	1090	3270	81,720.28	24.99	0.67

Table 2d
Summary of MBI parameters quoted the literature.

Studies	Sensor & Spatial resolution		Parameters for linear SE						Real-world dimensions
			N _d	d _{min}	S _{min}	S _{max}	Δs	N _s	
Units	m		–	°	pixels	pixels	pixels	–	m
Huang and Zhang (2011)	GeoEye-1	2	4/8	45/22.5	2	22	5	5	4–44
Huang and Zhang (2012)	Ikonos	1	4	0	2	52	5	11	2–52
	WorldView-2	2							4–44
Tang et al. (2013)	Ikonos	1	4	–	2	52	5	11	2–52
	QuickBird-2	2.4							4.8–124.8
Huang et al. (2014)	QuickBird-2	2.4	4	45	2	32	5	7	4.8–76.8
Wang et al. (2016)	ZY-3	2.5	4	0	2	65	7	10	5–162.5
Zhang et al. (2016)	GeoEye-1	2	8	22.5	2	22	5	5	4–44
	WorldView-2	2							
Li et al. (2017)	PAN/MS		4	–	2	52	5	11	
	QuickBird-2	0.6/2.4							1.2–124.8
	Pléiades	0.5/2.0							1–104
Ding et al. (2018)	PAN/MS		4	0	–	–	–	50	
	WorldView-2	0.5/2							–
	GF-2	1/4							–
	GF-1	2/8							–
You et al. (2018)	GaoFen2	1	4	–	–	–	–	7	4–36
Bi et al. (2019)	QuickBird-2	0.6	4	0	2	42	5	9	1.2–25.2
	WorldView-2	0.5							1–21
	GaoFen-2	0.8							1.6–33.6

shadow areas (≈5–7%) and vegetation (1–2%). Similar proportions of each labelled class were recorded in each sample region. These statistics explain why it is challenging to collect enough samples for the minority classes (shadow areas and vegetation) using a simple random sample strategy, as these classes have a much lower chance of being sampled. Samples for bare soil had a much higher mean segment size than the other classes. Samples for artificial surfaces had a consistent mean segment size of ≈35 m² across sample regions. Shadow areas and vegetation exhibited the smallest mean segment sizes of ≈20–24 m².

Regarding sample size, a minimum of 50 per class is recommended as a rule of thumb (Congalton, 2004; Congalton and Green,

2008). However, 200 segments (i.e. 4 classes \times 50 samples per class) represents a very small proportion (0.13%) of the total number of segments in the scene (150,290). Therefore, a total of 3270 samples were selected, equivalent to approximately 2% of the number of segments in the scene (see Table 2c) (De Luca et al., 2019). The samples were randomly split for training ($2/3$) and validation ($1/3$) of the ML classifiers (Fig. 1f), following Grippa et al. (2017).

2.3.4. Separability of classification features

The separability of the spectral and geometric classification features of the LC classes, and consequently their implied importance in the classification stage, was computed using the M-statistic (Kaufman and Remer, 1994), where μ is the mean value and σ is the standard deviation of the classification feature value for different classes. M-statistics were computed using the randomly selected labelled samples using the formula:

$$M = \frac{|\mu_1 - \mu_2|}{\sigma_1 + \sigma_2} \quad (3)$$

The M-statistic expresses the difference in the mean (i.e. the signal) normalised by the sum of the standard deviation (i.e. the noise) (De Luca et al., 2019). When $M < 1$, classes significantly overlap and the ability to separate the regions is poor; when $M > 1$, class means are well separated and relatively easily discriminated. Previously this technique has been applied to both pixel-based classification (Kumar et al., 2017) and OBIA (De Luca et al., 2019).

2.3.5. Classification

Random Forests (RF) has been shown to perform best in OBIA, usually followed by Support-Vector Machines (SVM) (Ma et al., 2017a,b). RF is an ensemble non-parametric learning technique that generates a number of random decision trees (DTs), each returning a classification label for each segment, which are then aggregated such that the class with the most 'votes' is assigned to each segment (Breiman, 2001). The DTs are trained using the same parameters, but on different training sets. Ensemble classifiers are based on the premise that a set of classifiers performs better than an individual classifier (Rodriguez-Galiano et al., 2012). In this study, five ML-algorithms were implemented: K-Nearest Neighbours (KNN), Shark Random Forests (SRF), SVM, RF, and DT. RF is the focus of the study, whilst other classifiers were implemented for comparative purposes. The best performing classifier (SRF using only the spectral means in the training stage, with a maximum of 200 trees in the forest, an OOB ratio of 0.66, and all 3270 samples) was applied to the segmented output of the full scene and metrics for each LC class determined. Classifier performance was evaluated based on the generated confusion matrices from which OA, producer's accuracy (PA), user's accuracy (UA), and F-score were calculated.

2.4. MBI for building detection

The original MBI algorithm and its post-processing framework were implemented in MATLAB by Bi et al. (2019). The scripts implement the major steps of MBI as per Huang & Zhang (2011), and the major steps of the post-processing framework, including MBI, area and LWR thresholds, as well as noise reduction. The scripts were implemented using MATLAB (version R2019a) and require the Image Processing Toolbox and the Mapping Toolbox. The original scripts were amended to change image format (.bmp to.tif), automation of raster metadata input, both panchromatic imagery and colour composites accepted as an input, outputting the MSI feature image as well as the MBI feature image, corrections to the calculation of the attributes of each raster image object, amendment of the length-width condition, correction of masking, and addition of Otsu thresholding (Otsu, 1979) on the MBI feature image. The input of the scripts is a panchromatic or multispectral image, whilst the outputs include the MBI/MSI feature images and the post-processed MBI building map, in GeoTIFF format. The MBI-based analysis was carried out using the 2018 pansharpened image to allow direct comparison with the OBIA results, as well as on the two panchromatic images from 2008 to 2018, in order to carry out MBI-based building change detection. Most MBI studies created reference maps by manually labelling samples through visual interpretation (You et al., 2018). For the pansharpened imagery, the vector reference maps created for the sample regions in the OBIA process were reclassified (i.e. 1 = building, and 0 = non-building (shadow areas, vegetation, or bare soil)), and converted to raster format (Fig. 1g). For the panchromatic imagery, reference maps were created by segmenting the panchromatic band for sample region S1 (LSMS parameters 5, 15, 30) and labelling each segment. A separate script was used to quantitatively evaluate the accuracy of the output, comparing the binary reference map with the MBI building map, and to return several widely accepted pixel-based accuracy metrics based on those reported by various MBI studies (Congalton, 1991; Song and Haithcoat, 2005; Congalton and Green, 2008; Rutzinger et al., 2009; Tang et al., 2013; Huang et al., 2014, 2017; Li et al., 2017; Gavankar and Ghosh, 2018; You et al., 2018; Ding et al., 2018; Bi et al., 2019).

2.4.1. MBI and post-processing parameters

There are various parameters associated with implementing the MBI that have been reported in the literature. These include Number of orientations of linear SE, Starting orientation angle of linear SE, Length of linear SE, Binarized MBI threshold, Minimum area criteria, and Maximum length-width ratio criteria (see Table 2d). Please see Appendix B for more detailed information on the calculation of these parameters.

2.4.2. Parameter optimisation

Using the analysis of MBI parameters (detailed in Appendix B) as a starting point, the parameters were systematically optimised for sample region S1 of the 2018 pansharpened imagery. The optimised parameters were independently tested on sample regions S2 and S3 for the same image. The final optimal MBI and post-processing parameters for sample region S1 of the 2018 pansharpened image (Table 2e, Table 3a), were then used to process the full scene, with an execution time of 3 h 39 min 27 s, and an MBI threshold of 0.1875

applied. Subsequently, the parameters for the 2018 panchromatic imagery were also optimised, and applied to the 2008 panchromatic imagery, as it has the same 0.5 m spatial resolution. Furthermore, a comparison with the Otsu method of automatic image thresholding was performed.

3. Results

3.1. OBIA for LC mapping

Separability given by the M-statistic allowed classification features to be ranked by their ability to discriminate different LC classes. The spectral band averages (mean, median, mode) had values of $M > 1$, and are therefore much better for class separability than other spectral features (i.e. SD, variance, variety) which had values of $M < 0.36$ (Table S2). Geometric features had very low values ($M < 0.35$); the geometric feature with the largest M-statistic was the HWR of the orientated minimum bounding box with an average of 0.239, however this is still much lower than the separability computed for the spectral means. Therefore, the geometric features are not expected to be of use in the classification stage and may in fact increase confusion in the training stage, by increasing the number of classification features with poor class separability.

The RF classifier performed best in terms of overall accuracy and Kappa when there was a maximum of 200 trees in the forest. A sharp increase was seen in OA from 5 to 25 trees, after which OA plateaued around 86–87%, whilst the execution time increased linearly in proportion to the maximum number of trees (Fig. 2a).

The SRF classifier marginally outperformed RF in terms of both OA (88% vs. 86%), Kappa (84% v. 81%) and all Precision, Recall and F-score metrics for the four LC classes, although the execution time was approximately five times greater. The SRF classifier outperformed RF, SVM, DT and KNN, in terms of both OA and Kappa (Table S3). For the artificial surfaces class, SRF outperformed all other classifiers in terms of Precision and F-score. Each trained classifier was applied to sample region S1 to visually compare the outputs (Fig. 2b). SVM exhibits confusion between bare soil and shadow areas, as evidenced by the large misclassified area, whilst KNN exhibits confusion in vegetated areas, as large patches are misclassified as bare soil.

Higher OA, Kappa, and F-scores for all four LC classes were achieved when training samples from all three sample regions were used in the training stage, rather than using samples from one or a combination of two sample regions. This increase in accuracy may be due to a larger number of training samples being used in the training stage, or it may be due to the enhanced accuracy anticipated when using samples that are well distributed in the study area. In the previous tests, the samples were split ($\frac{2}{3}$ for training, $\frac{1}{3}$ for validation) to enable comparison with other classifiers that do not have internal accuracy assessment functionality.

However, RF uses a bagging-approach to build the forest of decision trees through sampling with replacement. Each tree is trained using a different random sample set of approximately $\frac{2}{3}$ of the full dataset (Cutler et al., 2007). The remaining $\frac{1}{3}$ of the samples are used to calculate the impartial out-of-bag (OOB) error. Tests were conducted to vary the OOB ratio from 0 to 1 to determine the optimum ratio; the SRF documentation recommends 0.66. In this test all classification features were used, and all samples were used in the training (3,270). As the OOB error ratio is increased from 0.1 the overall accuracy and Kappa increase. This is expected since as the OOB error ratio is increased, a larger proportion of the samples are kept aside for training. An OOB error ratio of 0.66 (OA 93.52%) was selected in agreement with the recommendation by the original author of the algorithm (Breiman, 2001).

As computation of the variable importance of the RF classification features is not currently implemented in OTB, individual features were tested to determine their importance in the training stage. The spectral means provided the highest OA when used in isolation (mean 90.67%, median 88.35%, mode 86.51%). The remaining features all provided OA less than 76% and K less than 70%. The geometric features (area, perimeter, PP, SI, HW) performed poorly (OA: 40–60%), with HW being the best performing geometric feature (OA: 61.62%). Different combinations of classification features were also tested. Highest OA was achieved when all classification features were included (93.52%). When only the geometric features were used, the model did not perform as well as when only the spectral features were used (OA 75.08% vs. 92.14%). When using the spectral mean and variance (the default features computed for each segment by the LSMS algorithm), OA of 91.04% was achieved, whilst when using the mean and variance alone achieved OA of 90.67% and 70.03% respectively. It is time-consuming to compute the additional spectral features (8 per band) and geometric features (5) for every segment, especially for large imagery. It is not clear that the observed increase in accuracy (2.85% difference in OA for all classification features vs. only spectral mean) is valid, or whether it is due to redundancy in the classification features. Sufficiently accurate results can be achieved by using a single classification feature, the segment's mean pixel value for each spectral band (OA: 90.67%, Kappa: 87.43%), and therefore only this single feature was used in the final classification.

The final classified land cover map is shown in Fig. 2c. Land cover class statistics, including mean segment area and surface coverage, are provided in Table 3a. To compute only the area and number of buildings within the mine-clearance polygons, a 50 m buffer was generated and used to clip the land cover map (Fig. 2d). This was to account for the inaccuracy in the collection method of the coordinates for mine-clearance polygons and their subsequent misalignment with real-world features, and to define a single polygon by which to extract the land cover statistics. Whilst the total area of the 50 m buffer is 4,114,622.27 m² (Table 3b), the total area of the 59 clearance polygons was 3,042,862.77 m², and the total reported area cleared by the HALO Trust was 2,386,723 m².

The confusion matrix and accuracy metrics for each land cover class are given in Table 3c and Fig. 2e. The confidence index

Table 2e
Optimal MBI and post-processing parameters for sample region S1 of the 2018 pansharpened image.

N_d	d_{min}	s_{min}	s_{max}	Δs	N_s	t_{MBI}	t_A	t_{LWR}
4	38	4	144	20	8	0.2174	105	10

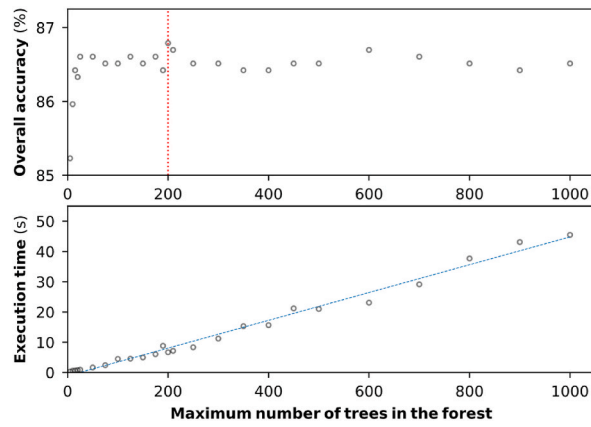


Fig. 2a. Impact of varying the maximum number of trees in the forest from 5 to 1000 on the overall accuracy (top), and the execution time (bottom).



Fig. 2b. Classified LC maps of sample region S1 from the 2018 pansharpened image, including SRF, RF, SVM, DT and KNN [Imagery source: U.S. Department of State © 2018 DigitalGlobe NextView License.].

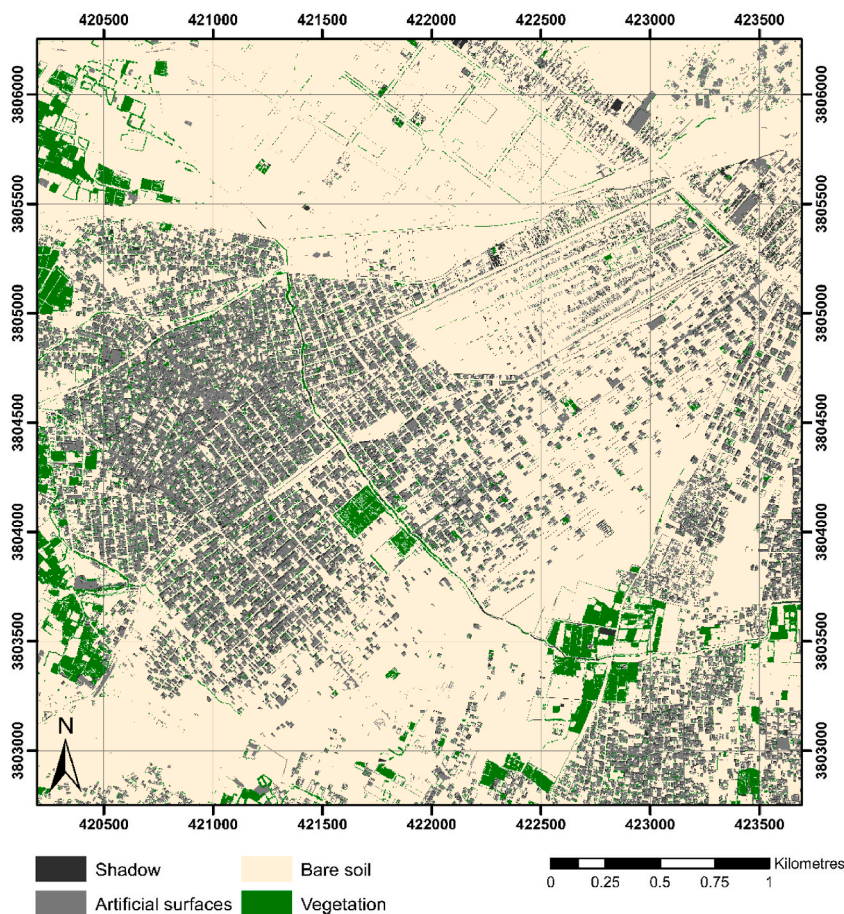


Fig. 2c. Land cover map derived from the 2018 pansharpened WorldView-3 imagery, using the SRF classifier in OTB. Classification output for areas displayed in Fig. 1e are displayed in Fig. S1 [Imagery source: U.S. Department of State © 2018 DigitalGlobe NextView License.].

assigned to each segment indicates the proportion of votes during the classification stage for the majority class (Fig. 2f). The artificial surfaces class had the highest confidence at 0.71, whilst the vegetation class had the lowest confidence at 0.47 (Fig. 2e).

3.2. MBI for building detection

The MBI building maps derived from the 2018 pansharpened WorldView-3 and the 2008/2018 panchromatic WorldView-1 imagery are shown in Fig. 2g and Fig. 2h respectively. The raster MBI building maps were clipped using the 50 m buffer for the clearance polygons.

The overall accuracy of the 2008 panchromatic image building map is very high (99.72%) (Table 3d). This is perhaps because the buildings in the reference map for sample region S1 make up a very small proportion of the total pixels in the scene (0.72%). One method to potentially improve the accuracy assessment would be to use more than one sample region as a reference map. Alternatively, sample regions with equal proportion of buildings and non-buildings should be selected.

The area of detected buildings was determined by counting the number of pixels labelled as buildings and multiplying by the pixel area per the spatial resolution (Table 3e). To calculate the number of buildings detected, the MBI building maps were vectorised and the number of objects counted. The change in built-area within the mine-clearance polygons, pre- and post-clearance, was determined by comparing the results from the 2008 and 2018 MBI building maps. An increase in built-area of 553,215 m² was seen during this 10-year period, whilst the number of building objects increased almost six-fold from 676 to 3895. The 2018 pansharpened image was acquired in July, whilst the 2018 panchromatic image was acquired later in October. Despite this a greater number of buildings are detected in the earlier acquired pansharpened imagery, a difference of 39,377.68 m² and 672 building objects. This may not equate to real change but is perhaps a result of using different MBI parameters for different images with different characteristics. Comparing the 2008 panchromatic and 2018 pansharpened MBI building maps, we see a greater increase in built-area of 592,592.68 m², and an

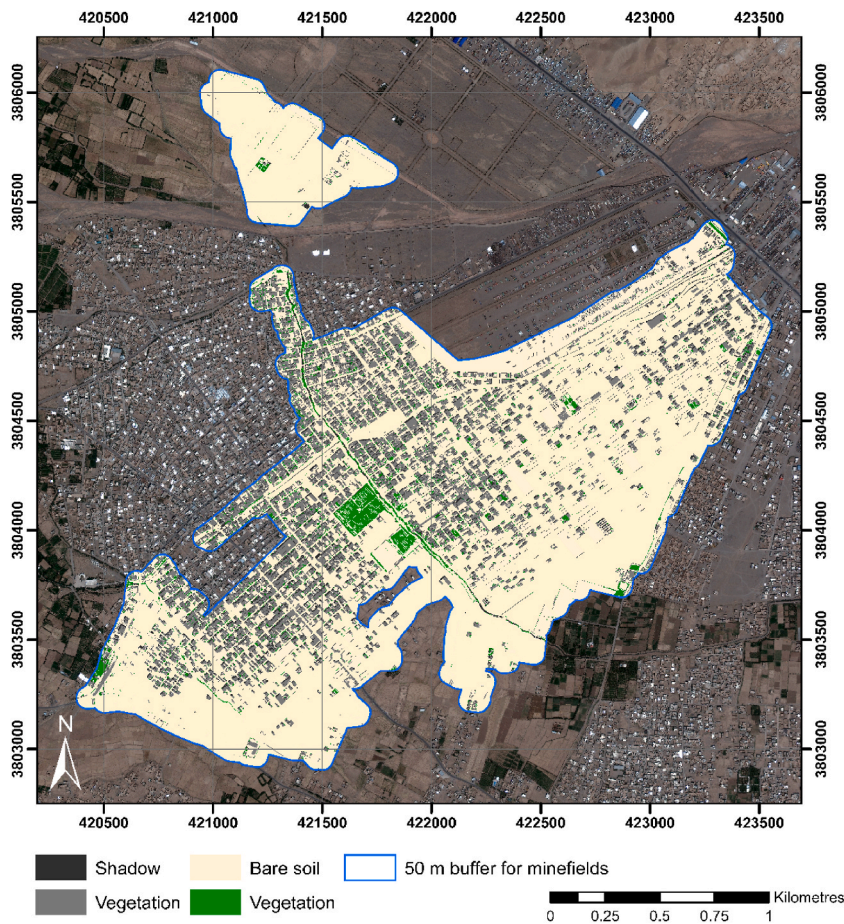


Fig. 2d. Land cover map clipped to 50 m buffer of clearance polygons, overlaid on the contrast enhanced panchromatic image [Imagery source: U.S. Department of State © 2018 DigitalGlobe NextView License].

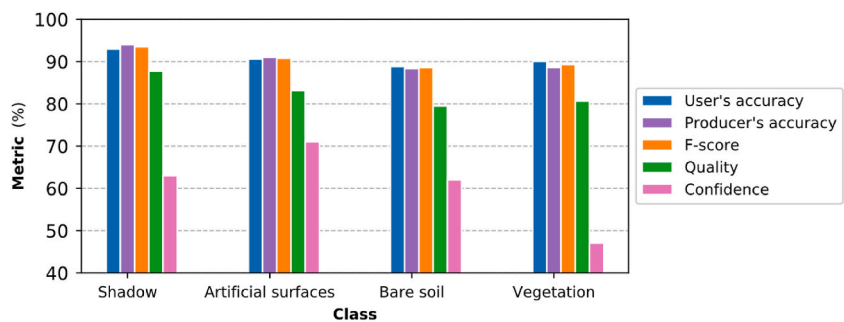


Fig. 2e. Accuracy metrics for each land cover class.

almost seven-fold increase in the number of building objects from 676 to 4567.

A choropleth map visualises the proportional change in built-area per clearance polygon, calculated by comparing the MBI building maps derived from the 2008 and 2018 panchromatic imagery (Fig. 2i). Mine-clearance areas which were closest to the existing suburb of Jebraïl have experienced the most development over the 10-year period.

4. Discussion

4.1. OBIA LC classification

Post-clearance land cover determination for the purposes of M&E of the impact of mine-clearance activities, was achieved by implementing an open-source, semi-automatic OBIA workflow, using VHR (0.28 m) imagery acquired in 2018, six years after clearance

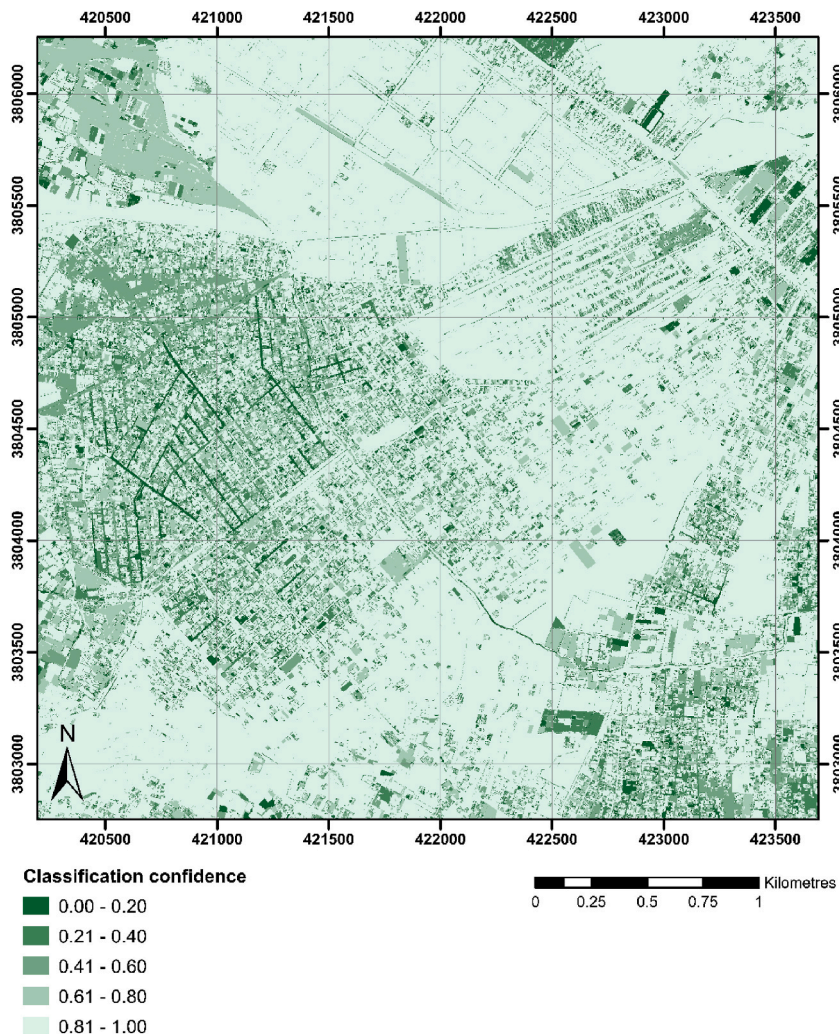


Fig. 2f. Confidence map for the SRF classification [Imagery source: U.S. Department of State © 2018 DigitalGlobe NextView License.].

activities were completed. Optimisation of the segmentation parameters by trial-and-error, albeit time-consuming, led to good discrimination of real-world objects. A minimum segment size equivalent to approximately 8 m^2 successfully eliminated noise. However, individual buildings were often represented by multiple segments, due to their complex physical structure and spectral response. No quantitative assessment of segmentation accuracy was made in this study; the output was assessed by visual interpretation and this remains the recommended method (Kaufman and Remer, 1994; Drăguț et al., 2014; De Luca et al., 2019). Future work could investigate the implementation of unsupervised and supervised methods of segmentation accuracy assessment in open-source software (Clinton et al., 2010; Costa et al., 2018; Ye et al., 2018). A limitation of the workflow was the time-consuming tile-wise segmentation step for large datasets, using LSMS in OTB. New segmentation algorithms based on super-pixels, using a recently developed add-on in GRASS GIS (Kanavath and Metz, 2017), have been shown to reduce computational time from over 5 h to 13 min for WorldView-2 scenes with 8 bands and 12.2 million pixels (Csillik, 2017). GRASS GIS may have been a suitable alternative choice of software, since it has had other recent enhancements for OBIA (Grippa et al., 2017).

A second limitation of the OBIA workflow was the significant manual intervention required to collect training/validation samples, also highlighted in similar studies; this remains a challenge to be overcome by future research into the automation of OBIA workflows (Grippa et al., 2017). In terms of the transferability of the OBIA workflow to different study areas in Afghanistan, if the imagery has the same spatial resolution and similar features, then the same segmentation parameters could be used, however, a new set of samples for training/validation would be required. Although ten spectral, five geometric and three MBI-index-based features were tested as training inputs in this study, only the spectral mean for each band was required to produce accurate results. By removing all other classification features, data redundancy was eliminated, and processing time significantly reduced. Other grey-level co-occurrence matrix (GLCM) textural features or digital surface models (DSMs) could be investigated in future, as well as using feature selection methods to optimise the feature subset (Ma et al., 2017b; Lebourgeois et al., 2017; Yang et al., 2019; De Luca et al., 2019). Inclusion of DSMs in the training stage would significantly aid discrimination of features with different heights, reducing the confusion between

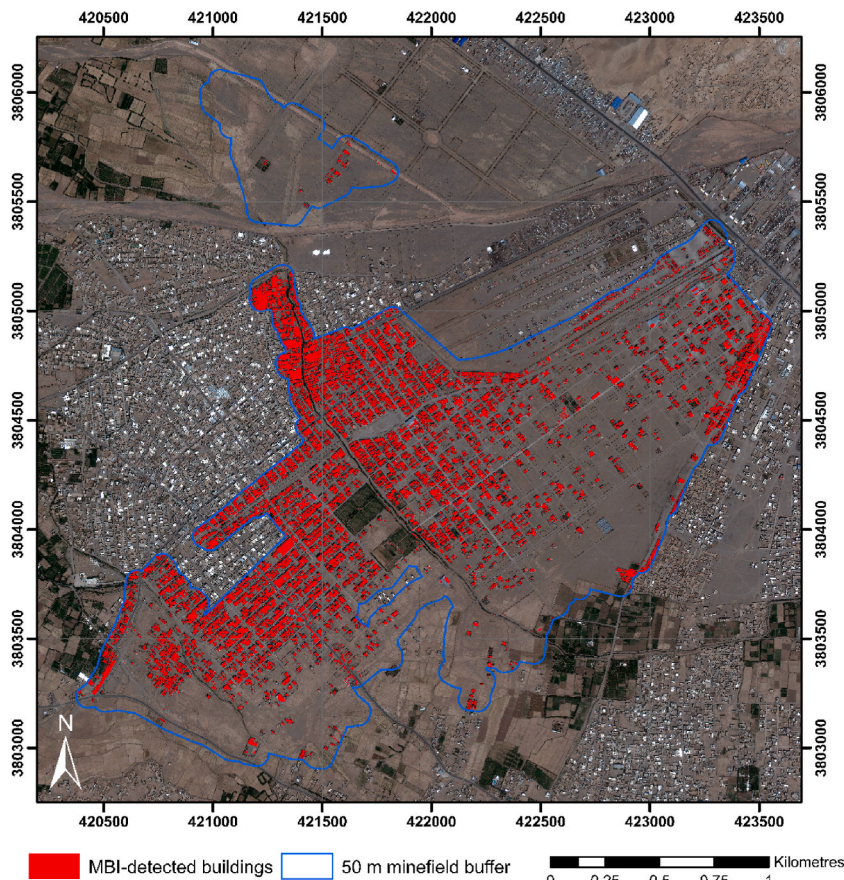


Fig. 2g. MBI building map derived from the 2018 pansharpened WorldView-3 imagery [Imagery source: U.S. Department of State © 2018 DigitalGlobe Next-View License.].

spectrally similar rooftops and bare soil. However, VHR DSMs for remote areas in developing countries such as Afghanistan are not available. With regards to feature selection methods, future work could implement RF with variable importance functionality.

Several studies confirmed that the default parameters in OTB for training and classification processes provide optimal results (Immitzer et al., 2016; Trisasongko et al., 2017; De Luca et al., 2019), however, as shown in this study, by optimising parameters such as the maximum number of trees in the forest, the accuracy metrics can be improved. Both versions of the RF classifier tested in this study were very fast, requiring less than 10 s, whilst the SVM classifier took significantly longer; the SRF classifier was found to give highest OA. Future studies could investigate the combination of multiple classifiers (Du et al., 2012). The most common false positive and false negative detections in the classification stage were a result of confusion between buildings and bare soil, and shadow areas and vegetation, also reported by De Luca et al. (2019), due to the spectral similarity of the classes. The accuracy of individual classes can be assessed by UA/PA values: shadow areas performed best (92.97/94.00%), whilst bare soil performed worst (88.83/88.33%). However, in terms of the confidence index computed in the classification stage, the artificial surfaces class performed best (71%), whilst vegetation performed worst (47%). It is very difficult to compare the results of this study, as no previous OBIA studies have been carried out for equivalent peri-urban environments in the same geographic location.

4.2. MBI building detection

An unsupervised adapted MBI-based approach, based on the original MBI methodology (Huang and Zhang, 2011) was implemented in MATLAB to determine change detection of buildings within the mine-clearance polygons from 2008 to 2018. Binary building/non-building maps were produced, with associated area and count metrics for detected buildings, and accuracy assessment. In terms of spatial resolution, previous studies focused on datasets with spatial resolution of 1–2 m, whilst the most recent studies used VHR 0.5 m WorldView-2 imagery (Bi et al., 2019). This study has shown that the method can be effectively applied to both panchromatic 0.5 m WorldView-1 and pansharpened 0.28 m WorldView-3 imagery covering a 12.25 km² study area in Afghanistan. To the best of our knowledge, this study is the first to apply the MBI to WorldView-3 imagery specifically, and to this unique type of

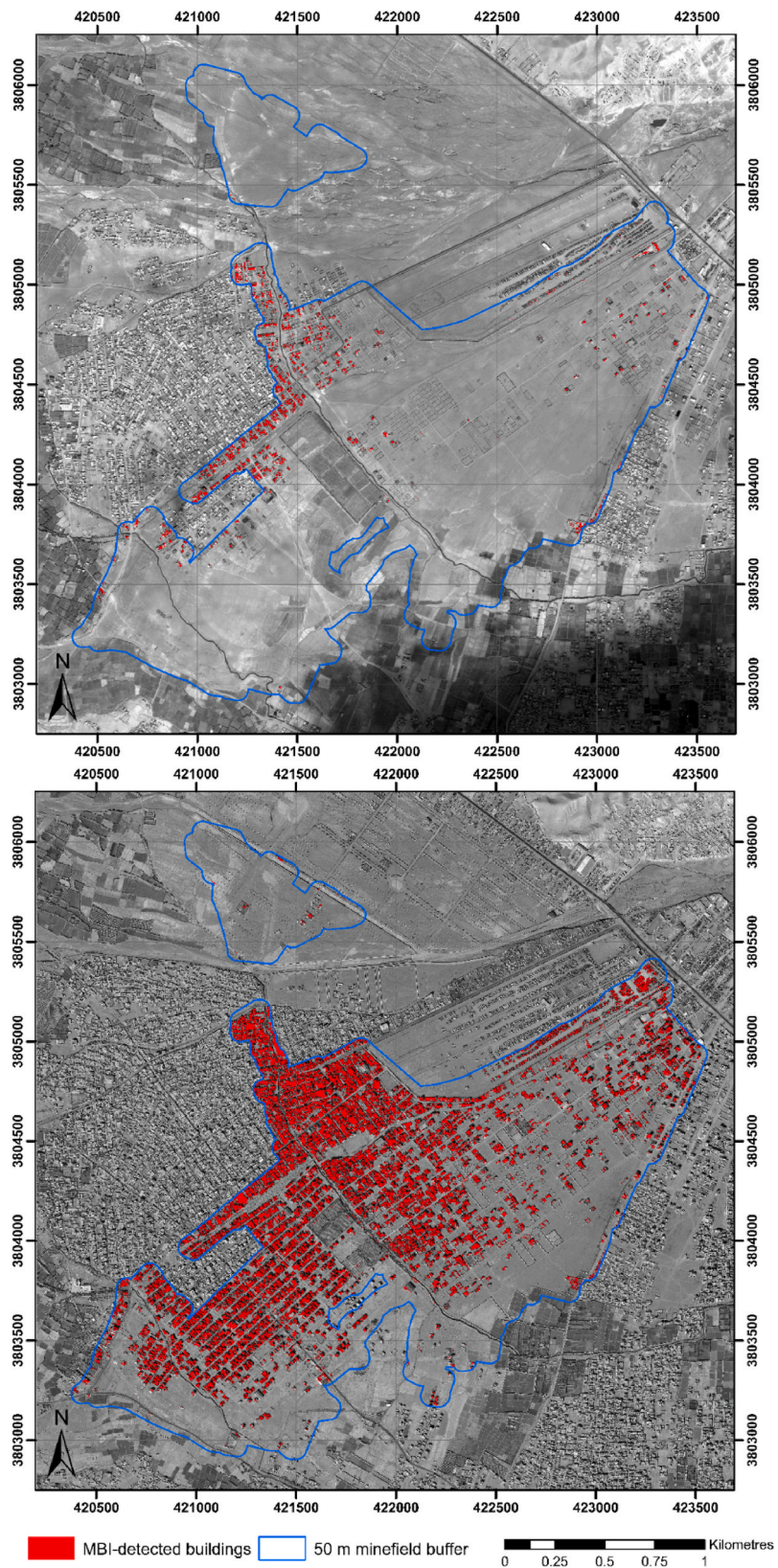


Fig. 2h. MBI building map derived from the 2008 (top) and 2018 (bottom) panchromatic WorldView-1 imagery [Imagery source: U.S. Department of State © 2008, 2018 DigitalGlobe NextView License.].

peri-urban environment. Previous studies focused on developed cities with high-rise buildings, such as Wuhan and Hangzhou in China (Huang and Zhang, 2011, 2012), although the method was later extended to rural, mountainous and agricultural areas by including shadow, spectral (e.g. Normalised Difference Vegetation Index (NDVI)) and shape constraints (Huang et al., 2017). The results indicated good performance for unsupervised, automatic building extraction from VHR imagery, with UA/PA in the range of 75–85% and Kappa coefficient in the range of 68–80%. The accuracies reported in this study are slightly lower than the original study which reported producer's accuracy of 82.8–93.1%, user's accuracy 93.6–98.0%, and Kappa coefficient of 77.7–91.0%. The sensitivity of the MBI parameters were analysed in the experiments, and following recommendations for the parameter setting are summarised as follows:

- i. Number of orientations of the SE, Nd: Results verified that the use of a linear SE with four orientations was effective in discriminating roads and buildings, in agreement with previous studies.
- ii. Starting orientation of the SE, dmin: This study performed novel analysis on the angle of orientation of the linear SE and found that the performance of the method improved when this parameter was calibrated in accordance with buildings and structures in the image.
- iii. Sizes of the SE, smin: Δs: smax: The study confirms that high accuracies are obtained when the lengths of the SEs are consistent with the actual dimensions of buildings in the scene. These parameters are dependent upon the spatial resolution and the size of features and should therefore be tuned to the specific dataset.
- iv. Binarized MBI threshold, tMBI: This parameter was shown to balance commission and omission errors (Fig. S2), examples of which were shown in Fig. S3 and Fig. S4, in agreement with previous studies (Huang and Zhang, 2011). The threshold must be tuned dependent upon the contrast of each dataset and the nature of features in the image. A small value is suggested in order to avoid a high omission error: a range from 0.21 to 0.44 was used in this study.
- v. Minimum area condition, tA: In this study the threshold was set at 105 corresponding to 8.5 m². This parameter should be set per the characteristics of the dataset and its features.
- vi. Maximum LWR condition, tLWR: The suggested value of the parameter is in the range of 5–10 in agreement with previous studies (Huang et al., 2017). As this threshold is a ratio, it is applicable to different datasets and different image scenes since the characteristic shapes of buildings are relatively consistent.

The MBI approach makes a basic assumption that all buildings have bright rooftops due to high reflectance and high contrast due to adjacent shadows. However, this assumption is not always valid, particularly in complex environments such as in this study, where some buildings exhibit very similar reflectance to areas of tarmac or bare soil and are very closely situated. However, the MBI is unsupervised and processes large imagery relatively fast and accurately, indicating potential for processing of large volumes of VHR imagery from different sensors.

4.2.1. Using the MBI index as a classification feature in OBIA

A test was conducted to assess whether the inclusion of the MBI index in the OBIA classification stage would increase the accuracy. Three classification features based on the MBI index were appended to the segments, including the number of pixels which had an MBI index of 0, the number of pixels with an MBI index of 1, and the percentage of the pixels within each segment which have an MBI index of 1. When all three MBI-based classification features are included in the training stage, OA/Kappa increased from 90.67%/87.43%–92.20%/89.49%. When only the MBI percentage index was included, OA/Kappa increased slightly to 90.83%/87.65%. By utilising the MBI-derived information in the OBIA training stage, in addition to the spectral means, the accuracy of the classification can be slightly improved. However, running both the MBI and OBIA processes involves many manual processing steps, for not a significant accuracy improvement.

4.3. Comparison of workflows

OBIA and MBI workflows applied to the same 2018 pansharp image provided remarkably similar results (Table 4a), with the total area and number of detected buildings differing by only 1.2% and 0.6% respectively.

Quantifying the number of buildings on the cleared land is more complex than determining the area. As a result of the OBIA workflow, real-world objects may be represented by multiple segments, dependent upon the segmentation stage. Thus, the counts recorded for each class are likely to represent a large over-estimation of the actual number of objects in the scene; the initial number of segments in the artificial surfaces class was 16,695. In order to make a direct comparison with the results from the MBI approach, any spatially contiguous segments were merged, reducing the count to 4,594, in close agreement with the MBI detection results (Table 4a). However, challenges remain, as this method has almost certainly merged separate real-world building objects into a single segment. For instance, a row or block of buildings may now be recognised as a single building, thus leading to potential under-estimation of the actual number of buildings in the scene. In order to assess the accuracy of the number of buildings detected, alternative object-based, rather than pixel-based, methods of accuracy assessment could be investigated (Ye et al., 2018). Another way to estimate the number of buildings would be to assume that one building may cover an area of 120 m², and to divide the total area; however, this method may not be any more accurate as it is purely an estimation.

In terms of accuracy, the artificial surfaces class extracted through OBIA outperformed the MBI-based building detection in terms of all metrics except OA (Table 4b); however, it must be noted that the OA for the OBIA method incorporates errors resulting from the remaining three classes. Despite the OBIA method appearing to be more accurate than MBI for building detection, it must be considered that the MBI method is unsupervised and does not require training data. Thus, if the objective is only to extract the built-up area, the MBI offers a fast, unsupervised approach with high accuracy; however, the parameters must be finely tuned to the specific

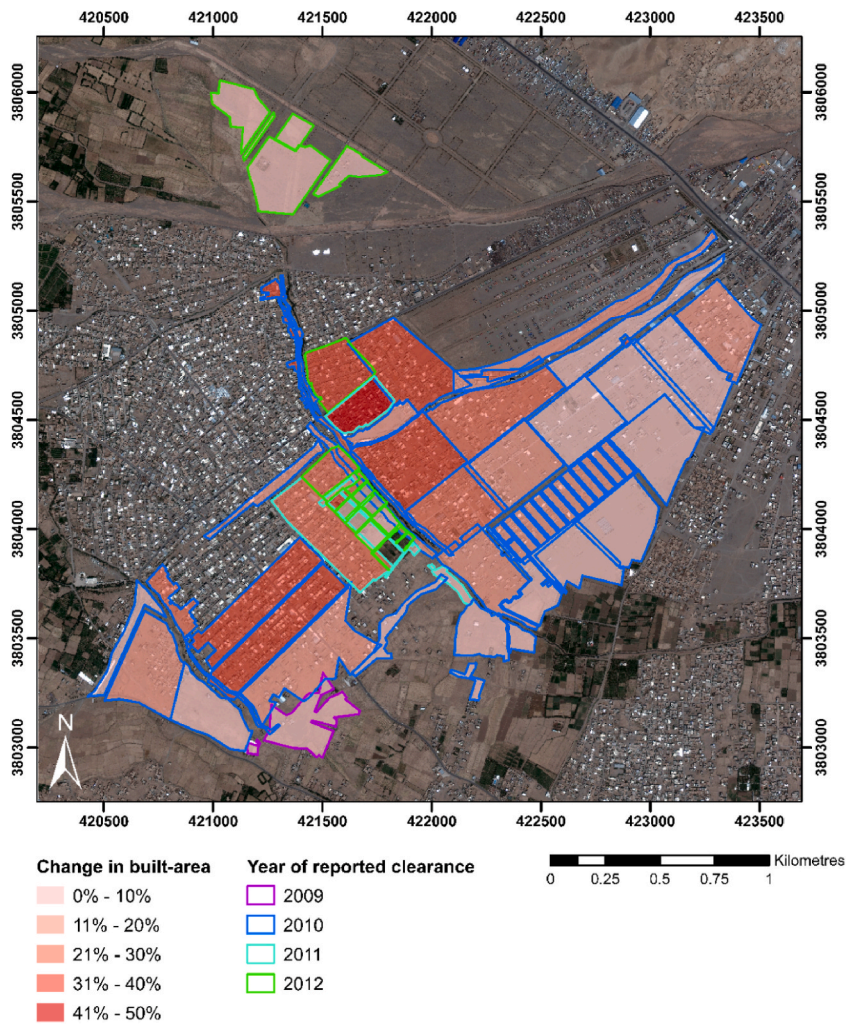


Fig. 2i. Multivariate choropleth map to indicate the proportional change in built-area from 2008 to 2018, and the year of reported clearance (2009–2012). Data is overlaid on the 2018 pansharpened RGB image for context [Imagery source: U.S. Department of State © 2008, 2018 DigitalGlobe NextView License.].

Table 3a
Land cover class statistics for full scene.

Predicted class	No. of segments	Total area, m ²	Mean segment area, m ²	Coverage (%)
Shadow areas	35,257	712,135.37	20.20	5.81
Artificial surfaces	45,073	1,787,819.36	39.66	14.59
Bare soil	47,859	8,969,590.18	187.42	73.21
Vegetation	22,101	782,388.26	35.40	6.39
Total	150,290	12,251,933.16	–	100.00

Table 3b
Land cover class statistics for clipped area.

Predicted class	No. of segments	Total area, m ²	Mean segment area, m ²	Coverage (%)
Shadow areas	11,345	251,548.47	22.17	6.11
Artificial surfaces	16,695	643,660.28	38.55	15.64
Bare soil	13,662	3,069,364.40	224.66	74.60
Vegetation	5604	150,049.12	26.78	3.65
Total	47,306	4,114,622.27	–	100.00

Table 3c

Confusion matrix for SRF classification. Classes are defined as: 0 = shadow areas, 1 = artificial surfaces, 2 = bare soil, 3 = vegetation.

		Reference				Total	User's accuracy
		0	1	2	3		
Predicted	0	846	5	10	49	910	92.97%
	1	1	819	84	0	904	90.60%
	2	13	71	795	16	895	88.83%
	3	40	5	11	505	561	90.02%
Total		900	900	900	570	3270	
Producer's accuracy		94.00%	91.00%	88.33%	88.60%		
F-score		93.48%	90.80%	88.58%	89.30%		
Quality		87.76%	83.15%	79.50%	80.67%		
Confidence		63.00%	71.00%	62.00%	47.00%		
Overall accuracy		90.67%					
Kappa		87.43%					

Table 2d

Accuracy metrics for the MBI building maps.

Image date	Image type	Accuracy metrics (%)					
		OA	PA	UA	Q	F	K
2008	Panchromatic	99.72	78.63	81.70	66.85	80.13	79.99
2018	Panchromatic	87.51	75.30	77.91	62.05	76.58	68.06
2018	Pansharpened	91.46	84.65	79.44	69.43	81.96	76.37

Table 3eArea and number of buildings detected in the MBI building maps. Coverage is a percentage of the clipped area, 4,114,622.27 m².

Image date	Image type	Total area, m ²	No. of objects	Mean object area, m ²	Coverage, %
2008	Panchromatic	58,705.00	676	86.84	1.43
2018	Panchromatic	611,920.00	3895	157.10	14.87
2018	Pansharpened	651,297.68	4567	142.61	15.83

dataset and geographic area in order to achieve good results. A summary of the advantages and disadvantages of each workflow is provided in [Table 4c](#).

M&E of the impact of mine-clearance activities requires timely acquisition and analysis of spatial and temporal information. Mapping output generated from OBIA and MBI analysis may be beneficial to M&E teams at humanitarian demining charities such as the HALO Trust, who depend on current geographic information for determining and quantifying land use changes. Furthermore, the results of this study provide a clear indication of the impact of mine-clearance in Jebtrail, evidenced by the quantified change in built-area.

4.4. Limitations

Only panchromatic imagery was available pre-clearance, prior to 2009, from the DigitalGlobe portal. It is not possible to perform OBIA on panchromatic imagery since the low spectral resolution will not provide sufficient class separability. Consequently, it was not possible to perform object-based change detection (OBCD) to quantify changes in LC. Future studies on different study areas should investigate the application of OBCD, as object-based methods, rather than pixel-based, may have more potential for change detection from VHR imagery ([Hussain et al., 2013](#)).

Jebtrail has a very low proportion of vegetation within the mine-cleared areas, however if the workflow was applied to a different area with a large amount of vegetation, indices such as the NDVI could be utilised in addition to the spectral bands in both the segmentation and classification stages. This could increase the accuracy, especially in areas where different species and layers of vegetation are spatially close ([De Luca et al., 2019](#)). Currently, only panchromatic or pansharpened true colour composites are available for The HALO Trust to access; if multispectral data was available in the future, a hierarchical classification schema with different types of vegetation or artificial surfaces could be implemented ([Lebourgeois et al., 2017](#)). However, studies have shown that for OBIA LC mapping in urban environments, the new spectral bands of WorldView-2 (Coastal, Yellow, Red Edge, NIR-2) did not improve on the accuracy achieved by the benchmark established from GeoEye-1 (Red, Green, Blue, NIR) ([Aguilar et al., 2013](#)). Inclusion of the NDVI, computed from the red and NIR bands, would significantly reduce the confusion between vegetation and shadow classes; spectral

indices have been shown to have a higher impact on separability than reflectance (Lebourgeois et al., 2017). However, MBI studies have shown that the inclusion of the NDVI mask in the post-processing stage is not critical for building extraction from urban areas and that satisfactory results are still obtained (Huang and Zhang, 2012), but should the method be applied to highly vegetated areas, then this step must be included to eliminate commission errors due to detection of bright vegetation.

5. Conclusions

Identifying buildings and mapping the spatial distribution of different types of LC is of great practical significance for demining organisations, such as the HALO Trust, to monitor and evaluate the impact of their work, by assessing change and the growth of a population in a specific area over time. Two independent methodologies were investigated in this study: OBIA for LC mapping and MBI for building detection. To map the LC of the peri-urban environment of Jebrail, on the outskirts of the city of Herat in Afghanistan, after mine-clearance activities from 2009 to 2012, a supervised OBIA approach was implemented using a VHR WorldView-3 pansharpened true colour composite acquired in 2018. The image was segmented using the LSMS algorithm and the RF classifier was applied. Different parameters and spatial distribution of training samples were tested to analyse the model's performance. The workflow was able to map LC with OA of 90.67% and Kappa coefficient of 87.43%. Specifically, for the 'artificial surfaces' LC class, PA/UA of 91.00/90.60% was achieved, and a total built-area of 643,660.28 m² detected.

To detect buildings at the study site, an alternative unsupervised approach based on the MBI was implemented using MATLAB. Two VHR (0.5 m) WorldView-1 panchromatic images acquired in 2008 and 2018 were analysed and binary building maps produced. Parameters were optimised and their sensitivity analysed. Comparing the output maps to reference maps, PA/UA of 78.63/81.70% and 75.30/77.91% were attained. The built area at the study site was found to increase from 58,705 to 611,920 m², over the ten-year period, indicating a significant increase in the number of people resident in the area.

Consequently, the two methods were directly compared, and whilst OBIA was found to be more accurate than MBI, with PA/UA of 91.00/90.60% versus 84.65/79.44%, the actual area of detected buildings was remarkably similar. Thus, if the sole objective is to detect buildings, then the MBI offers a novel unsupervised approach that requires no training data; however, the parameters must be finely tuned to the dataset and features at the specific geographic location. Alternatively, if the objective of the study is to map LC, then the more well-established OBIA workflow is the appropriate choice; however, training samples are not transferable, and the analyst must collect new samples for each dataset.

Funding

This work was supported by funds allocated to the University of Glasgow from the Global Challenges Research Fund (GCRF) via the Scottish Funding Council (SFC). Historical, unclassified, VHR commercial satellite imagery and derived products were provided to The HALO Trust, as a not-for-profit organisation (NPO), by the U.S. Government National Geospatial-Intelligence Agency (NGA) under the G-EGD's NextView license.

Ethics statement

The authors have considered the ethics of this research from its inception and adhere to the duties outlined within the journal publishing ethics guidelines.

CRedit authorship contribution statement

Jennifer Killeen: Conceptualization, Methodology, Software, Formal analysis, Investigation, Validation, Visualization, Writing – original draft. **Luan Jaupi:** Conceptualization, Resources, Data curation, Writing – review & editing. **Brian Barrett:** Conceptualization, Supervision, Funding acquisition, Visualization, Writing – review & editing.

Declaration of competing interest

The authors declare that they have no known competing financial interests or personal relationships that could have appeared to influence the work reported in this paper.

Supplementary data

Supplementary data to this article can be found online at <https://doi.org/10.1016/j.rsase.2022.100766>.

Table 4a
Comparison of OBIA/MBI building/artificial surfaces detection results.

Image date	Image type	Method	Total area, m ²	No. of objects	Mean object area, m ²	Coverage, %
2018	Pansharpened	MBI	651,297.68	4567	142.61	15.83
2018	Pansharpened	OBIA	643,660.28	4594	134.88	15.64

Table 4b
Comparison of accuracy metrics for OBIA/MBI methods.

Image date	Image type	Method	Accuracy metrics (%)					
			OA	K	PA	UA	Q	F
2018	Pansharpened	OBIA	90.67	87.43	91.00	90.60	83.15	90.80
2018	Pansharpened	MBI	91.46	76.37	84.65	79.44	69.43	81.96

Table 4c
Comparison of the workflows implemented in this study.

Method	Advantages	Disadvantages
OBIA	<ul style="list-style-type: none"> - Open-source software (QGIS/OTB) - Easy to add further steps in the workflow - Only one classification feature required (spectral means) - Rapid classification - Vector output - Multiple land cover classes - Processing segments rather than pixels 	<ul style="list-style-type: none"> - Time-consuming to determine the optimum segmentation parameters - Segmentation step is time-consuming for large VHR imagery - Time-consuming and labour-intensive manual sample collection (supervised method) - Requires multiple spectral bands to ensure adequate class separability
MBI	<ul style="list-style-type: none"> - Unsupervised method: no samples are required for training - Fast computation for large VHR imagery. - Multi-scale and multi-directional processing - Doesn't require visual interpretation or knowledge of the study area - Requires only a single grayscale raster image 	<ul style="list-style-type: none"> - MATLAB requires a license - Format demands a certain level of programming ability from the user to run the scripts and change inputs/outputs and parameters - Difficult to add new steps in the scripts without programming knowledge - Parameters must be tuned for each dataset and geographic location - Time-consuming to create reference maps through which to evaluate the accuracy - Single land cover class detected (buildings) - Raster output

Appendix A. Mine Clearance activities in Jebrail

During the 1980s, Jebrail was a large, flat, open area, south of the highway traversing east to west from Herat to Islam Qala at the Iranian border. The Afghan Army were stationed to the north of the highway, whilst the existing villages including Jebrail were occupied by local people sympathetic to the Mujahideen. The Mujahideen attacked the Afghan Army base, which resulted in Soviet and Afghan government forces reciprocating on a regular basis using tanks and armoured personnel carriers (APCs). This prompted the Mujahideen to lay anti-tank (AT) mines in defence, concentrated at canal crossing points around Jebrail. Most of the mines laid were acquired by the Mujahideen through Iran and designed to be difficult to detect, consisting of minimum metal, thus requiring the use of very sensitive metal detectors and/or mechanical demining units (MDUs), depending upon the burial depth.

During the 1990s until 2008, mine clearance was carried out by various Herat-based agencies, such as the UN coordinated body, Mine Action Coordination Centre of Afghanistan (MACCA), and the Western Area Mine Action Centre (AMAC). Three Afghan non-governmental organisations (NGOs) were also involved in clearance activities, including the Mine Detection Centre (MDC), using mine detection dogs (MDD), the Demining Agency for Afghanistan (DAFA) and the Organisation for Mine Clearance and Afghan Rehabilitation (OMAR). They cleared a total area of 4,612,542 m², finding and safely destroying 116 AT mines (The HALO Trust, 2011a), after which the cleared land was returned to local people. Since 2008, Jebrail has seen a steady rise in population due to a large increase in returning refugees and IDPs from Herat. The cleared land was divided into plots and sold to the new population. Despite prior clearance, there were a significant number of accidents (16 deaths, 15 injuries, and 15 missed mines), both on cleared land and adjacent uncleared land. The HALO Trust, the world's largest humanitarian mine clearance organisation carried out a full re-clearance of the entire suburb, including further suspect areas, during two programmes (March–December 2011 (The HALO Trust, 2011a; 2011b); January–June 2012 (The HALO Trust, 2012)). Both manual mine clearance teams (MCTs) and MDUs were utilised in each programme (Figure A1). Jebrail was experiencing a major construction boom and many compounds were already constructed or under construction. MCTs cleared around the base of walls and foundations to prevent damage by MDUs. MDUs were used to clear the remaining areas; they are more efficient around collapsed buildings, in narrow irrigation canals, in areas with high metal concentration and in preparing ground for cultivation. In November 2011, the HALO Trust reported having cleared 2.15 million m² at Jebrail, finding a total of 8 AT mines. A further 7000 m² was cleared in December 2011, and a further 126,120 m² in 2012. The final total cleared area reported by the HALO Trust was 2,386,723 m²; a total of 11 AT mines and 670 ERW (UXO and bullets) were recovered.



Fig. A1. Manual mine clearance teams (MCTs) and Mechanical demining units (MDUs) working in Jebraïl, Afghanistan. Source: The HALO Trust.

In 2011, the HALO Trust reported that 1180 families were resident on or very close to suspect ground, or were using the land for communal grazing, and would directly benefit from the clearance. At the time, it was not possible to account for future beneficiaries, who bought and constructed upon the land. The local Municipality decreed that all the land was to be made available for housing, and the HALO Trust estimated that the final population of the completed clearance area may exceed 5000 families (The HALO Trust, 2011b). The HALO Trust interviewed local villagers in Jebraïl during the clearance regarding the problem of mines. They reported that the clearance has significantly impacted their lives, seeing an increase in trade, construction, and property value since the HALO Trust clearance began. Previously, much of Jebraïl was uninhabitable due to landmines, but the impact of the clearance has resulted in a huge amount of construction, including schools, houses, roads and mosques. Today, Jebraïl is home to almost 60,000 former refugees and IDPs (The HALO Trust, 2011a).

Appendix B. MBI Parameters

B1 Number of orientations of linear SE

Huang & Zhang (2011) showed that varying the number of orientations for the linear SE, N_d , from 4 to 8 did not significantly improve the accuracy but did significantly increase the computational time. All the studies referenced in Table 2d used 4 orientations with an interval of 45° , except Zhang et al. (2016) who used 8 with an interval of 22.5° . As a result, 4 orientations were used in this study.

B2 Starting orientation angle of linear SE

All studies cited in Table 2d used a starting orientation angle, d_{min} , of 0° or 45° ; none of the papers reported the impact of varying this parameter on the OA. A value of 0° or 45° would be appropriate if features in the image were orthogonal with the image axes, however this is not the case for the imagery in this study. To determine the appropriate value, the orientation angle of every building in the reference maps was measured using its orientated minimum bounding box (Figure B1). Most buildings were found to be orientated at orthogonal angles of approximately 52° or 142° (Figure B2), in line with the road network. In MATLAB, an angle of 0° is measured from the equivalent of due east, whilst in QGIS, an angle of 52° is measured from due north, and therefore it should be subtracted from 90° to convert it to the equivalent angle in MATLAB. Therefore, setting $d_{min} = 38^\circ$ and $N_d = 4$ would generate linear SEs through orientations of $38^\circ/83^\circ/128^\circ/173^\circ$. The linear SE function in MATLAB creates a linear SE that is symmetric with respect to the neighbourhood centre, with approximate length in pixels and angle in degrees set by the user.

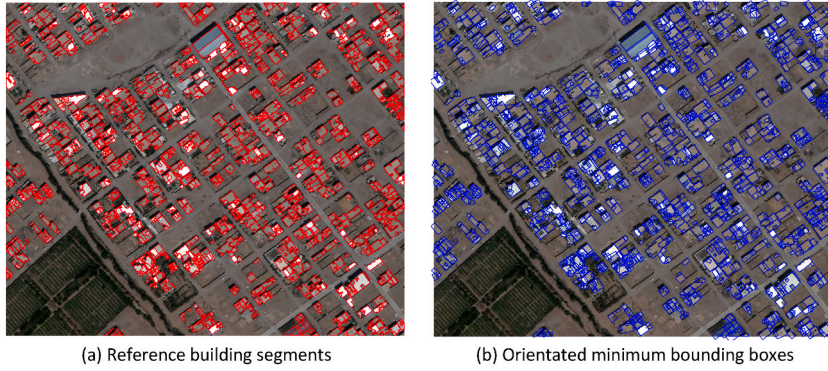


Fig. B1. Examples of the (a) reference building segments generated by the LSMS segmentation stage and manually labelled, and (b) their respective orientated minimum bounding boxes. [Imagery source: U.S. Department of State © 2018 DigitalGlobe NextView License.]

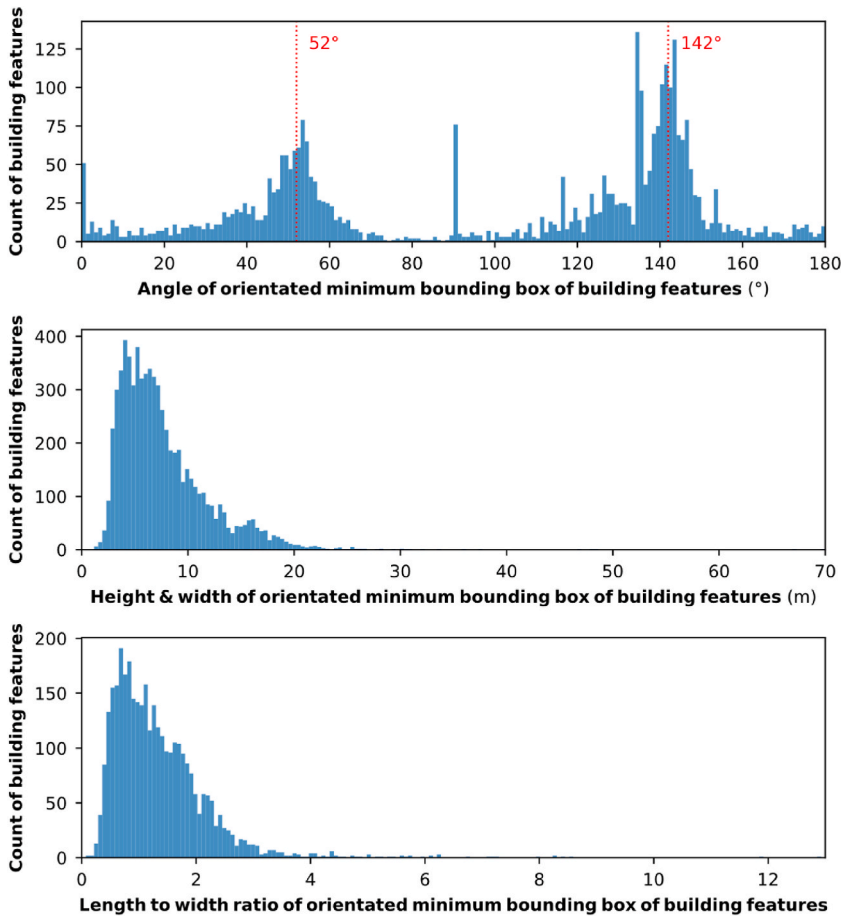


Fig. B2. Frequency histograms for the angle, height and width, and length-to-width ratio of the orientated minimum bounding box of building features from the reference maps (3436 objects) for the three sample regions of the 2018 pansharpened imagery.

B3 Length of linear $SE(s_{min}, s_{max}, \Delta s, N_s)$

The limits of scale of the linear SE (s_{min}, s_{max}) should be set according to the spatial resolution and the actual sizes of buildings in the study area. Therefore, these parameters need to be changed according to each image. The number of different scales, N_s , is given by:

$$N_s = \frac{s_{max} - s_{min}}{\Delta s} + 1 \# \tag{b1}$$

where Δs is the interval. Table 2d includes scale parameters and spatial resolutions from recent publications, which were used to guide the choice of these parameters in this study. In the original publication on MBI by Huang & Zhang (2011), they reported buildings in their study area as ranging from 6 to 60 m (informal settlements to large apartments), which with 2 m spatial resolution corresponds to

3 to 30 pixels, and therefore guided their choice of parameters as $2 \leq s \leq 22, \Delta s = 5$. They showed that high accuracies were achieved when the sizes of the SE were consistent with actual buildings in the scene. Furthermore, Wang et al. (2016) investigated the impact of varying Δs (30, 15, 7, 5, 2). An interval of 30 was found to create stripes in the MBI feature image, whilst an interval of 2 contained large omission errors; an interval of 7 was observed to give the best results. You et al. (2018) provided a method of estimating the appropriate number of scales, from the maximum and minimum lengths of building in the scene, L_{max} and L_{min} , using the formula:

$$N_s = \left(\frac{L_{max} - L_{min}}{5} \right) + 1. \# \tag{b2}$$

For the 2008/2018 panchromatic imagery with spatial resolution 0.5 m, to create linear SEs with the same real-world sizes per Zhang et al. (2016) (i.e. 4 - 44 m), the corresponding parameters are $8 \leq s \leq 88, \Delta s = 10, N_s = 9$. For the 2018 pansharpened imagery with spatial resolution 0.28 m, the corresponding parameters are $4 \leq s \leq 166, \Delta s = 18, N_s = 10$. From orientated minimum bounding boxes of the building features, the minimum and maximum lengths were computed (1.37–69.79 m). However, most buildings were in the range of 2–24 m (Figure B2). This would correspond to 4–48 pixels for 0.5 m resolution, or 4–84 pixels for 0.28 m resolution.

B4 Binarized MBI threshold (t_{MBI})

The normalised MBI index ranges from [0, 1]. Buildings have larger MBI values as they have a brighter reflectance relative to their surroundings. The initial MBI building map result is obtained by applying a threshold, t_{MBI} . Generally, a low threshold results in small OE, but large CE, and similarly a high threshold results in large OE, but small CE (Huang and Zhang, 2011). A small value should be used to avoid a high OE and to keep more building candidates for the subsequent shape filters. One of the challenges in the application of MBI is identifying the appropriate threshold. Table B1 lists thresholds reported in the literature. Huang et al. (2017) reiterated that the parameter should be fine-tuned according to the different test datasets, and that the preferred threshold can be selected in terms of the Q-score to balance the PA and UA. Huang et al. (2014) experimented with t_{MBI} from 0.1 to 0.9, with an interval of 0.1. They showed that the CE decreases and the OE increases gradually with increasing values of t_{MBI} since more components have been removed with a higher threshold. The balance point for t_{MBI} was approximately 0.3 for the specific imagery. Jiménez et al. (2017) experimented with t_{MBI} values of 0.00, 0.20, 0.39, 0.59, and 0.78. A range of values from 0.00 to 0.75 were tested in this study to determine the optimum threshold for the dataset.

Table B1
Summary of post-processing parameters quoted in publications.

Publication	Post-processing thresholds			Spatial resolution	Real-world area
	t_{MBI}	t_A	t_{LWR}		
Units	–	pixels	–	m	m ²
Huang & Zhang (2011)	1.5/2/3	30	9.6	2	120
Huang & Zhang (2012)	0.5–3	–	–	1/2	–
Huang et al. (2014)	0.3	30	–	2.4	172.8
Zhang et al. (2016)	–	30	9.6	2	120
Huang et al. (2017)	0.04–0.12	4/9	7–10	2.4/2	23.04/36
Gavankar & Ghosh (2018)	–	400–40,000	7	0.6	144–14,400
You et al. (2018)	1–6	20	>3 (3.5, 4, 5)	1	20
Bi et al. (2019)	0.45	30	5.6	0.6/0.5/0.8	10.8/7.5/19.2

B5 Minimum area criteria (t_A)

The minimum area threshold is used to remove small noisy features that are deemed too small to be buildings. The appropriate value for t_A should be less than the smallest building feature in the image to avoid erroneous removal of building features. Different studies have reported different thresholds (Table B1); however, this parameter should be tuned to the spatial resolution and size of features in the image. Analysing the building features from the reference maps, the minimum area is approximately 8 m², which corresponds to 100 pixels for 0.28 m resolution imagery. However, this minimum segment size is an artefact of the segmentation process, during which a minimum segment size of 100 pixels was specified. Therefore, this statistic may not accurately represent the actual minimum building area. For 0.5 m resolution imagery, 8 m² would correspond to 32 pixels.

B6 Maximum length-width ratio criteria (t_{LWR})

The maximum length-width ratio condition is used to remove long, narrow and elongated anisotropic features. As this conditional value is a ratio, it is independent of the spatial resolution used in the study and is only constrained by the features within the specific scene. Studies have reported values in the range of 3–10 (Table B1). Following the method outlined by Bi et al. (2019), the orientated minimum bounding boxes were used to calculate the length-width ratio, so that objects at different orientations can be described more accurately. Most building features in the reference maps had $t_{LWR} < 5$.

References

- Aguilar, M.A., Saldaña, M.M., Aguilar, F.J., 2013. GeoEye-1 and WorldView-2 pan-sharpened imagery for object-based classification in urban environments. *Int. J. Rem. Sens.* 34 (7), 2583–2606. <https://doi.org/10.1080/01431161.2012.747018>.
- Baatz, M., Schäpe, A., 2000. Multiresolution segmentation: an optimization approach for high quality multi-scale image segmentation. In: Strobl, J., Blaschke, T., Griesbner, G. (Eds.), *Angewandte Geographische Informations-Verarbeitung*, vol. XII. Wichmann Verlag, Karlsruhe, Germany, pp. 12–23.
- Bhaskaran, S., Paramananda, S., Ramnarayan, M., 2010. Per-pixel and object-oriented classification methods for mapping urban features using Ikonos satellite data. *Appl. Geogr.* 30 (4), 650–665. <https://doi.org/10.1016/j.apgeog.2010.01.009>.
- Bi, Q., Qin, K., Zhang, H., Zhang, Y., Li, Z., Xu, K., 2019. A multi-scale filtering building index for building extraction in very high-resolution satellite imagery. *Rem. Sens.* 11 (5), 482. <https://doi.org/10.3390/rs11050482>.
- Blaschke, T., 2010. Object based image analysis for remote sensing. *ISPRS J. Photogrammetry Remote Sens.* 65 (1), 2–16. <https://doi.org/10.1016/j.isprsjprs.2009.06.004>.
- Blaschke, T., Lang, S., Lorup, E., Strobl, J., Zeil, P., 2000. Object-Oriented image processing in an integrated GIS/remote sensing environment and perspectives for environmental applications. In: Cremers, A., Greve, K. (Eds.), *Environmental Information for Planning, Politics and the Public*, vol. 2. Metropolis Verlag, Marburg, pp. 555–570.
- Breiman, L., 2001. Random forests. *Mach. Learn.* 45 (1), 5–32. <https://doi.org/10.1023/A:1010933404324>.
- Christophe, E., Inglada, J., 2009a. Object counting in high-resolution remote sensing images with OTB. In: Presented at the 2009 IEEE International Geoscience and Remote Sensing Symposium, vol. 4. IEEE, Cape Town, South Africa, pp. 737–740. <https://doi.org/10.1109/IGARSS.2009.5417482>.
- Christophe, E., Inglada, J., 2009b. Open source remote sensing: increasing the usability of cutting-edge algorithms. *IEEE Geosc. Rem. Sens. Soc. Newslet.* 35 (5), 9–15.
- Cleve, C., Kelly, M., Kearns, F.R., Moritz, M., 2008. Classification of the wildland–urban interface: a comparison of pixel- and object-based classifications using high-resolution aerial photography. *Comput. Environ. Urban Syst.* 32 (4), 317–326. <https://doi.org/10.1016/j.compenvurbysys.2007.10.001>.
- Clinton, N., Holt, A., Scarborough, J., Yan, L., Gong, P., 2010. Accuracy assessment measures for object-based image segmentation goodness. *Photogramm. Eng. Rem. Sens.* 76 (3), 289–299. <https://doi.org/10.14358/PERS.76.3.289>.
- Comaniciu, D., Meer, P., 2002. Mean shift: a robust approach toward feature space analysis. *IEEE Trans. Pattern Anal. Mach. Intell.* 24 (5), 603–619. <https://doi.org/10.1109/34.1000236>.
- Congalton, R.G., 1991. A review of assessing the accuracy of classifications of remotely sensed data. *Rem. Sens. Environ.* 37 (1), 35–46. [https://doi.org/10.1016/0034-4257\(91\)90048-B](https://doi.org/10.1016/0034-4257(91)90048-B).
- Congalton, R.G., 2004. Putting the map back in map accuracy assessment. In: Lunetta, R.S., Lyon, J.G. (Eds.), *Remote Sensing and GIS Accuracy Assessment*, first ed. CRC Press, Boca Raton, FL, USA, pp. 1–11.
- Congalton, R.G., Green, K., 2008. *Assessing the Accuracy of Remotely Sensed Data: Principles and Practices*, second ed. CRC Press, Boca Raton, FL, USA.
- Costa, H., Foody, G.M., Boyd, D.S., 2018. Supervised methods of image segmentation accuracy assessment in land cover mapping. *Rem. Sens. Environ.* 205, 338–351. <https://doi.org/10.1016/j.rse.2017.11.024>.
- Cresson, R., Grizonnet, M., Michel, M., 2018. Orfeo ToolBox Applications. In: Baghdadi, N., Mallet, C., Zribi, M. (Eds.), *QGIS and Generic Tools*, vol. 1. Wiley.
- Cruz, I., Jaupi, L., Sequesseque, S.K.N., Cottray, O., 2018. Enhancing humanitarian mine action in Angola with high-resolution UAS IM. *J. Convent. Weap. Destruct.* 22 (3), 5.
- Csillik, O., 2017. Fast segmentation and classification of very high-resolution remote sensing data using SLIC superpixels. *Rem. Sens.* 9 (3), 243. <https://doi.org/10.3390/rs9030243>.
- Cutler, D.R., Edwards, T.C., Beard, K.H., Cutler, A., Hess, K.T., Gibson, J., Lawler, J.J., 2007. Random forests for classification in ecology. *Ecology* 88 (11), 2783–2792. <https://doi.org/10.1890/07-0539.1>.
- De Luca, G., N Silva, J.M., Cerasoli, S., Araújo, J., Campos, J., Di Fazio, S., Modica, G., 2019. Object-based land cover classification of cork oak woodlands using UAV imagery and orfeo ToolBox. *Rem. Sens.* 11 (10), 1238. <https://doi.org/10.3390/rs11101238>.
- Ding, Z., Wang, X.Q., Li, Y.L., Zhang, S.S., 2018. Study on building extraction from high-resolution images from MBI. *Int. Arch. Photogram. Rem. Sens. Spatial Inf. Sci. XLII-3*, 283–287. <https://doi.org/10.5194/isprs-archives-XLII-3-283-2018>. Beijing, China.
- Drăguț, L., Csillik, O., Eisank, C., Tiede, D., 2014. Automated parameterisation for multi-scale image segmentation on multiple layers. *ISPRS J. Photogrammetry Remote Sens.* 88, 119–127. <https://doi.org/10.1016/j.isprsjprs.2013.11.018>.
- Du, P., Xia, J., Zhang, W., Tan, K., Liu, Y., Liu, S., 2012. Multiple classifier system for remote sensing image classification: a review. *Sensors* 12 (4), 4764–4792. <https://doi.org/10.3390/s120404764>.
- FAS, 2020. Federation of American Scientists (FAS) Intelligence Resource Program (IRP), National Image Interpretability Rating Scale. <https://fas.org/irp/imint/niirs.htm>. (Accessed 20 August 2020).
- Fernández, M.G., López, Y.A., Arboleya, A.A., Valdés, B.G., Vaqueiro, Y.R., Andrés, F.L.H., García, A.P., 2018. Synthetic aperture radar imaging system for landmine detection using a ground penetrating radar on board a unmanned aerial vehicle. *IEEE Access* 6, 45100–45112.
- Frost, A., Boyle, P., Autier, P., et al., 2017. The effect of explosive remnants of war on global public health: a systematic mixed-studies review using narrative synthesis. *Lancet Public Health.* [https://doi.org/10.1016/S2468-2667\(17\)30099-3](https://doi.org/10.1016/S2468-2667(17)30099-3).
- Galletti, C.S., Myint, S.W., 2014. Land-use mapping in a mixed urban-agricultural arid landscape using object-based image analysis: a case study from maricopa, Arizona. *Rem. Sens.* 6 (7), 6089–6110. <https://doi.org/10.3390/rs6076089>.
- Gavankar, N.L., Ghosh, S.K., 2018. Automatic building footprint extraction from high-resolution satellite image using mathematical morphology. *Europ. J. Rem. Sens.* 51 (1), 182–193. <https://doi.org/10.1080/22797254.2017.1416676>.
- Grippa, T., Lennert, M., Beaumont, B., Vanhuyse, S., Stephenne, N., Wolff, E., 2017. An open-source semi-automated processing chain for urban object-based classification. *Rem. Sens.* 9 (4), 358. <https://doi.org/10.3390/rs9040358>.
- Grizonnet, M., Michel, J., Poughon, V., Inglada, J., Savinaud, M., Cresson, R., 2017. Orfeo ToolBox: open source processing of remote sensing images. *Open Geosp. Data, Software and Stand.* 2 (15), 1–8. <https://doi.org/10.1186/s40965-017-0031-6>.
- Huang, X., Zhang, L., 2011. A multidirectional and multiscale morphological index for automatic building extraction from multispectral GeoEye-1 imagery. *Photogramm. Eng. Rem. Sens.* 77 (7), 721–732. <https://doi.org/10.14358/PERS.77.7.721>.
- Huang, X., Zhang, L., 2012. Morphological building/shadow index for building extraction from high-resolution imagery over urban areas. *IEEE J. Sel. Top. Appl. Earth Obs. Rem. Sens.* 5 (1), 161–172. <https://doi.org/10.1109/JSTARS.2011.2168195>.
- Huang, X., Zhang, L., Zhu, T., 2014. Building change detection from multitemporal high-resolution remotely sensed images based on a morphological building index. *IEEE J. Sel. Top. Appl. Earth Obs. Rem. Sens.* 7 (1), 105–115. <https://doi.org/10.1109/JSTARS.2013.2252423>.
- Huang, X., Yuan, W., Li, J., Zhang, L., 2017. A new building extraction postprocessing framework for high-spatial-resolution remote-sensing imagery. *IEEE J. Sel. Top. Appl. Earth Obs. Rem. Sens.* 10 (2), 654–668. <https://doi.org/10.1109/JSTARS.2016.2587324>.
- Hussain, M., Chen, D., Cheng, A., Wei, H., Stanley, D., 2013. Change detection from remotely sensed images: from pixel-based to object-based approaches. *ISPRS J. Photogrammetry Remote Sens.* 80, 91–106. <https://doi.org/10.1016/j.isprsjprs.2013.03.006>.
- Ibrahim, N., Fahs, S., AlZoubi, A., 2021. April. Land cover analysis using satellite imagery for humanitarian mine action and ERW survey. *Multimod. Image Exploit. Learn.* 2021 11734, 1173402 (International Society for Optics and Photonics).
- Immitzer, M., Vuolo, F., Atzberger, C., 2016. First experience with sentinel-2 data for crop and tree species classifications in central europe. *Rem. Sens.* 8 (3), 166. <https://doi.org/10.3390/rs8030166>.
- Jiménez, L.I., Plaza, J., Plaza, A., 2017. Efficient implementation of morphological index for building/shadow extraction from remotely sensed images. *J. Supercomput.* 73 (1), 482–494. <https://doi.org/10.1007/s11227-016-1890-9>.
- Kaya, S., Leloglu, U.M., 2017. Buried and surface mine detection from thermal image time series. *IEEE J. Sel. Top. Appl. Earth Obs. Rem. Sens.* 10 (10), 4544–4552.

- Kanavath, R., Metz, M., 2017. GRASS GIS 7.6.2 Reference Manual: Addon - i.superpixels.Slic. Retrieved August 15, 2019, from <https://grass.osgeo.org/grass76/manuals/addons/i.superpixels.slic.html>.
- Kaufman, Y.J., Remer, L.A., 1994. Detection of forests using mid-IR reflectance: an application for aerosol studies. *IEEE Trans. Geosci. Rem. Sens.* 32 (3), 672–683. <https://doi.org/10.1109/36.297984>.
- Kumar, P.R., Prasad, R.S., Choudhary, A., Mishra, V.N., Gupta, D.K., Srivastava, P.K., 2017. A statistical significance of differences in classification accuracy of crop types using different classification algorithms. *Geocarto Int.* 32 (2), 206–224. <https://doi.org/10.1080/10106049.2015.1132483>.
- Lebourgeois, V., Dupuy, S., Vintrou, É., Ameline, M., Butler, S., Bégue, A., 2017. A combined random forest and OBIA classification scheme for mapping smallholder agriculture at different nomenclature levels using multisource data (simulated sentinel-2 time series, VHRS and DEM). *Rem. Sens.* 9 (3), 259. <https://doi.org/10.3390/rs9030259>.
- Lhomme, S., He, D.-C., Weber, C., Morin, D., 2009. A new approach to building identification from very-high-spatial-resolution images. *Int. J. Rem. Sens.* 30 (5), 1341–1354. <https://doi.org/10.1080/01431160802509017>.
- Li, S., Tang, H., Huang, X., Mao, T., Niu, Z., 2017. Automated detection of buildings from heterogeneous VHR satellite images for rapid response to natural disasters. *Rem. Sens.* 9 (11), 1177. <https://doi.org/10.3390/rs9111177>.
- Ma, L., Li, M., Ma, X., Cheng, L., Du, P., Liu, Y., 2017a. A review of supervised object-based land-cover image classification. *ISPRS J. Photogrammetry Remote Sens.* 130, 277–293. <https://doi.org/10.1016/j.isprsjprs.2017.06.001>.
- Ma, L., Fu, T., Blaschke, T., Li, M., Tiede, D., Zhou, Z., et al., 2017b. Evaluation of feature selection methods for object-based land cover mapping of unmanned aerial vehicle imagery using random forest and Support vector machine classifiers. *ISPRS Int. J. Geo-Inf.* 6 (2), 51. <https://doi.org/10.3390/ijgi6020051>.
- Ma, W., Wan, Y., Li, J., Zhu, S., Wang, M., 2019. An automatic morphological attribute building extraction approach for satellite high spatial resolution imagery. *Rem. Sens.* 11 (3), 337. <https://doi.org/10.3390/rs11030337>.
- Maathuis, B.H., 2003. Remote sensing based detection of minefields. *Geocarto Int.* 18 (1), 51–60.
- Makki, I., Younes, R., Francis, C., Bianchi, T., Zucchetti, M., 2017. A survey of landmine detection using hyperspectral imaging. *ISPRS J. Photogrammetry Remote Sens.* 124, 40–53.
- Michel, J., Youssefi, D., Grizonnet, M., 2015. Stable mean-shift algorithm and its application to the segmentation of arbitrarily large remote sensing images. *IEEE Trans. Geosci. Rem. Sens.* 53 (2), 952–964. <https://doi.org/10.1109/TGRS.2014.2330857>.
- NOAA, 2019. Afghanistan Climate Data. <https://library.noaa.gov/Collections/Digital-Docs/Foreign-Climate-Data/Afganistan-Climate-Data>. (Accessed 5 June 2019).
- Otsu, N., 1979. A threshold selection method from gray-level histograms. *IEEE Transact. Sys., Man, and Cyber.* 9 (1), 62–66. <https://doi.org/10.1109/TSMC.1979.4310076>.
- Pesaresi, M., Gerhardinger, A., Kayitakire, F., 2008. A robust built-up area presence index by anisotropic rotation-invariant textural measure. *IEEE J. Sel. Top. Appl. Earth Obs. Rem. Sens.* 1 (3), 180–192. <https://doi.org/10.1109/JSTARS.2008.2002869>.
- Polsby, D.D., Popper, R.D., 1991. The Third Criterion: compactness as a procedural safeguard against partisan gerrymandering. *Yale Law Pol. Rev.* 9 (2), 301–353.
- Rodríguez-Galiano, V.F., Ghimire, B., Rogan, J., Chica-Olmoa, M., Rigol-Sanchez, J.P., 2012. An assessment of the effectiveness of a random forest classifier for land-cover classification. *ISPRS J. Photogrammetry Remote Sens.* 67, 93–104. <https://doi.org/10.1016/j.isprsjprs.2011.11.002>.
- Rutzinger, M., Rottensteiner, F., Pfeifer, N., 2009. A comparison of evaluation techniques for building extraction from airborne laser scanning. *IEEE J. Sel. Top. Appl. Earth Obs. Rem. Sens.* 2 (1), 11–20. <https://doi.org/10.1109/JSTARS.2009.2012488>.
- Song, W., Haithcoat, T.L., 2005. Development of comprehensive accuracy assessment indexes for building footprint extraction. *IEEE Trans. Geosci. Rem. Sens.* 43 (2), 402–404. <https://doi.org/10.1109/TGRS.2004.838418>.
- Tang, Y., Huang, X., Zhang, L., 2013. Fault-tolerant building change detection from urban high-resolution remote sensing imagery. *Geosci. Rem. Sens. Lett. IEEE* 10 (5), 1060–1064. <https://doi.org/10.1109/LGRS.2012.2228626>.
- The HALO Trust, 2011a. Jebraïl UNMAS VTF Project, Q1 Interim Report, 1st March - 31st May 2011.
- The HALO Trust, 2011b. Jebraïl UNMAS VTF Project, Q2 Interim Report, 1st June - 31st August 2011.
- The HALO Trust, 2012. Jebraïl UNMAS VTF Proposal, Jebraïl 'Extra' Clearance, 1st January - 30st June 2012.
- The HALO Trust, 2020. Afghanistan. <https://www.halotrust.org/where-we-work/central-asia/afghanistan/>. (Accessed 20 August 2020).
- Trisasongko, B.H., Panuju, D.R., Paull, D.J., Jia, X., Griffin, A.L., 2017. Comparing six pixel-wise classifiers for tropical rural land cover mapping using four forms of fully polarimetric SAR data. *Int. J. Rem. Sens.* 38 (11), 3274–3293. <https://doi.org/10.1080/01431161.2017.1292072>.
- UN data, 2019. Afghanistan. <http://data.un.org/en/iso/af.html> (Accessed 20 August 2020).
- United States Institute of Peace, 2015. Political & Economic Dynamics of Herat by Jolyon Leslie, Peaceworks No. 107. <https://www.usip.org/sites/default/files/PW107-Political-and-Economic-Dynamics-of-Herat.pdf>. (Accessed 20 August 2020).
- Wang, S., Tian, Y., Zhou, Y., Liu, W., Lin, C., 2016. Fine-scale population estimation by 3D reconstruction of urban residential buildings. *Sensors* 16 (10), 1755. <https://doi.org/10.3390/s16101755>.
- Weng, Q., Quattrochi, D., Gamba, P.E. (Eds.), 2018. *Urban Remote Sensing*, second ed. CRC Press, Boca Raton, FL, USA.
- Xiangguo, L., Jixian, Z., 2017. Object-based morphological building index for building extraction from high resolution remote sensing imagery. *Acta Geod. Cartogr. Sinica* 46 (6), 724–733. <https://doi.org/10.11947/j.AGCS.2017.20170068>.
- Yang, L., Mansaray, L.R., Huang, J., Wang, L., 2019. Optimal segmentation scale parameter, feature subset and classification algorithm for geographic object-based crop recognition using multisource satellite imagery. *Rem. Sens.* 11 (5), 514. <https://doi.org/10.3390/rs11050514>.
- Ye, S., Pontius, R.G., Rakshit, R., 2018. A review of accuracy assessment for object-based image analysis: from per-pixel to per-polygon approaches. *ISPRS J. Photogrammetry Remote Sens.* 141, 137–147. <https://doi.org/10.1016/j.isprsjprs.2018.04.002>.
- You, Y., Wang, S., Ma, Y., Chen, G., Wang, B., Shen, M., Liu, W., 2018. Building detection from VHR remote sensing imagery based on the morphological building index. *Rem. Sens.* 10 (8), 1287. <https://doi.org/10.3390/rs10081287>.
- Zhang, Q., Huang, X., Zhang, G., 2016. A morphological building detection framework for high-resolution optical imagery over urban areas. *Geosci. Rem. Sens. Lett. IEEE* 13 (9), 1388–1392. <https://doi.org/10.1109/LGRS.2016.2590481>.